IMPROVED PERFORMANCES IN SUBSONIC FLOWS OF AN SPH SCHEME WITH GRADIENTS ESTIMATED USING AN INTEGRAL APPROACH

R. VALDARNINI[1,2]

[1] SISSA, Via Bonomea 265, I-34136, Trieste, Italy; valda@sissa.it
[2] Iniziativa Specifica QGSKY, Via Valerio 2, I-34127 Trieste, Italy

ABSTRACT

In this paper, we present results from a series of hydrodynamical tests aimed at validating the performance of a smoothed particle hydrodynamics (SPH) formulation in which gradients are derived from an integral approach. We specifically investigate the code behavior with subsonic flows, where it is well known that zeroth-order inconsistencies present in standard SPH make it particularly problematic to correctly model the fluid dynamics. In particular, we consider the Gresho–Chan vortex problem, the growth of Kelvin–Helmholtz instabilities, the statistics of driven subsonic turbulence and the cold Keplerian disk problem. We compare simulation results for the different tests with those obtained, for the same initial conditions, using standard SPH. We also compare the results with the corresponding ones obtained previously with other numerical methods, such as codes based on a moving-mesh scheme or Godunov-type Lagrangian meshless methods. We quantify code performances by introducing error norms and spectral properties of the particle distribution, in a way similar to what was done in other works. We find that the new SPH formulation exhibits strongly reduced gradient errors and outperforms standard SPH in all of the tests considered. In fact, in terms of accuracy, we find good agreement between the simulation results of the new scheme and those produced using other recently proposed numerical schemes. These findings suggest that the proposed method can be successfully applied for many astrophysical problems in which the presence of subsonic flows previously limited the use of SPH, with the new scheme now being competitive in these regimes with other numerical methods.

Key words: hydrodynamics – methods: numerical

1. INTRODUCTION

Application of computational fluid dynamics to many astrophysical problems has grown steadily over the years with advances in computational power, and it has now become a standard tool for studying the nonlinear evolution of baryonic structures in the universe.

There are two methods commonly used in numerical astrophysics for solving the Euler equation. The first method makes use of a spatial grid, either fixed (Stone & Norman 1992; Norman & Bryan 1999; Stone et al. 2008) or adaptive (Fryxell et al. 2000; Teyssier 2002; Norman 2005; Bryan et al. 2014). The second method is a Lagrangian mesh-free numerical scheme, known as smoothed particle hydrodynamics (SPH: Gingold & Monaghan 1977; Lucy 1977) in which particles are used to model fluid properties. Both methods have advantages and weaknesses that are specific to the numerical approach on which each method is based.

Because of its Lagrangian nature, SPH possesses very good conservation properties, moreover the method is free of advection errors present in mesh codes and is naturally adaptative because particle trajectories trace the mass. This latter feature is particularly useful in many astrophysical problems involving collapse of the structure under study.

The method, however, is not free from significant drawbacks and more specifically it has been found that in several hydrodynamical test cases there are significant differences between the results obtained using the two methods, with SPH failing to properly model the correct behavior (O'Shea et al. 2005; Agertz et al. 2007; Tasker et al. 2008; Wadsley et al. 2008; Mitchell et al. 2009; Junk et al. 2010; Read et al. 2010; Valcke et al. 2010).

More specifically, Agertz et al. (2007) found that SPH fails to resolve the formation of Kelvin–Helmholtz (KH) instabilities at fluid interfaces. This is strongly related to the fluid mixing properties of SPH as well as to the lack of a core entropy in non-radiative simulations of galaxy clusters, in contrast with what is found using mesh-based codes (Wadsley et al. 2008; Mitchell et al. 2009).

It is now widely recognized that the origin of these errors is due to two distinct problems, which are present in SPH. The first problem originates from the inconsistencies of standard SPH when dealing with steep density gradients at contact discontinuities, the so-called local mixing instability (LMI; Read et al. 2010), thereby suppressing the growth of KH instabilities at the fluid interfaces. The second problem is inherent in the discrete nature of SPH, in which a finite set of particles is used to model the fluid. The discretization implies the presence of a zeroth-order error in the momentum equation due to sampling effects (Read et al. 2010), the so-called E_0 error. This error can be reduced if one increases the number of neighbors N_n present within the kernel, but for the standard cubic spline kernel there is a threshold value for N_n beyond which a clumping instability develops thus degrading the convergence rate.

In view of the benefits of the SPH method previously outlined, there have been many attempts to eliminate or reduce these difficulties. Several solutions have been proposed, concerning the problem posed by the standard formulation at contact discontinuities.

One solution is to modify the equations, so that it is the pressure rather than the density that is smoothed (Ritchie & Thomas 2001; Read et al. 2010; Hopkins 2013; Saitoh & Makino 2013; Hu et al. 2014). On the other hand, Price (2008)

proposed the inclusion of a term of artificial conductivity (AC) in the SPH energy equation with the aim of smoothing the thermal energy across fluid interfaces and thus removing the associated entropy gap. This approach is similar to that used by Wadsley et al. (2008), who mimicked the effect of subgrid turbulence by adding a heat-diffusion term to the equations. The method, however, requires some care in the implementation of the conduction switches to avoid the risk of getting too much diffusion.

By performing a suite of hydrodynamical tests (Valdarnini 2012, hereafter V12) it has been found that the method yields consistent results when contrasted with those obtained using mesh-based codes. In particular (V12; Biffi & Valdarnini 2015), the level of core entropies produced in simulations of non-radiative galaxy clusters are now comparable with those of grid codes. Recently, Beck et al. (2016) have proposed a modification to the standard SPH code Gadget-II (Springel 2005), which incorporate the new AC term into the hydrodynamic equations.

Finally, other variants of SPH are based on Riemann solvers (Godunov-SPH: Inutsuka 2002; Cha et al. 2010; Murante et al. 2011), Voronoi tessellation techniques (Heß & Springel 2010), or the use of high-order dissipation switches (Read & Hayfield 2012).

The zeroth-order inconsistency is due to the inability of the SPH method to properly reproduce a constant function because of finite resolution (Dilts 1999; Liu et al. 2003), thus leading to poor gradient estimates (Read et al. 2010; McNally et al. 2012) and in turn affecting the momentum equations. Keeping these errors under control becomes problematic when dealing with subsonic flows, as in the case of subsonic turbulence (Bauer & Springel 2012) or with Rayleigh–Taylor instabilities (Abel 2011; García-Senz et al. 2012, V12).

A possible solution is to drastically increase the number of neighbors used in the simulation. In this case, the clumping instability can be avoided either by modifying the shape of the cubic spline kernel (Read et al. 2010) or by adopting (Dehnen & Aly 2012) the Wendland kernels (Wendland 1995). These kernels are characterized by the specific property of not being subject to clumping instabilities in the large N_n limit.

Another possibility is to consider other discretizations of the momentum equation (Morris 1996; Abel 2011) but this comes at the cost of losing energy and momentum conservation (Price 2012a), thus making the scheme of little use in practice.

Finally, to overcome the difficulties of SPH mentioned above, new numerical schemes have been proposed (Springel 2010; Duffell & MacFadyen 2011; Hopkins 2015; Schaal et al. 2015; Pakmor et al. 2016) that aim to retain the advantages of using both SPH and mesh-based codes. These new schemes are quite numerically complex and, in some cases, their space discretization does not seem to be optimal as required by forthcoming parallel computing systems consisting of several million cores (Schaal et al. 2015).

A satisfactory solution to the problem of zeroth-order inconsistency in SPH has been presented by García-Senz et al. (2012), who showed how the accuracy in gradient estimates can be greatly improved by calculating first-order derivatives by means of the evaluation of integrals and the use of matrix inversions. The resulting tensor scheme has been tested in a variety of hydrodynamical test cases (García-Senz et al. 2012; Rosswog 2015), showing significant improvements as compared with the standard formulation. A crucial feature of

the method is that it retains the Lagrangian nature of SPH, unlike previous attempts aimed at improving gradient accuracy.

Motivated by these findings, we here further investigate the performance of the new scheme, paying particular attention to its behavior in the regime of subsonic flows, where it has been found that standard SPH presents major difficulties.

The goal of this paper is to demonstrate that, for the hydrodynamical tests considered here, the new SPH formulation gives results with accuracy comparable to that of mesh-based codes. Thus, the new code can be profitably used for many astrophysical problems without the shortcomings of standard SPH. The main advantage of the new scheme is that it keeps its fully Lagrangian nature, while retaining a relative simplicity in its implementation as compared with new numerical schemes recently proposed.

The paper is organized as follows. In Section 2, we present the hydrodynamical method and the implementation of the integral-based approach. Some basic properties of the most widely used SPH kernels are briefly reviewed in Section 3. The results of the hydrodynamical tests are given in Section 4, where we consider the Gresho–Chan vortex problem, the development of KH instabilities, the statistic of driven subsonic turbulence and finally the Keplerian disk problem. Our main results and conclusions are summarized in Section 5.

2. HYDRODYNAMIC METHOD

This section reviews the basic features of SPH; for a comprehensive review, see Rosswog (2009) and Price (2012a).

2.1. Basic Equations

In SPH, the fluid is described within the solution domain by a set of N particles with mass m_i, velocity v_i, density ρ_i, and specific entropy A_i (we use the convention of having Latin indices denoting particles and Greek indices denoting the spatial dimensions). Here, we integrate the entropy per particle (Springel & Hernquist 2002) in place of the thermal energy per unit mass u_i (Hernquist & Katz 1989; Wadsley et al. 2004). The entropy A_i is related to the particle pressure P_i by $P_i = A_i \rho_i^\gamma = (\gamma - 1)\rho_i u_i$, where $\gamma = 5/3$ for a mono-atomic gas. The density estimate at the particle position r_i is given by

$$\rho_i = \sum_j m_j W(|r_{ij}|, h_i), \qquad (1)$$

where $W(|r_i - r_j|, h_i)$ is the interpolating kernel, which is zero for $|r_i - r_j| \geqslant \zeta h_i$ (Price 2012a). Since the kernel has compact support, the sum in Equation (1) is over a finite number of particles. The smoothing length h_i is implicitly defined by

$$h_i = \eta(m_i/\rho_i)^{1/D}, \qquad (2)$$

so that in two and three dimensions, respectively, $N_{nn}^{2D} = \pi(\zeta\eta)^2$ and $N_{nn}^{3D} = 4\pi(\zeta\eta)^3/3$ are the mean number of neighboring particles of particle i within a radius ζh_i. In principle, for a given parameter η, the solution of Equation (2) allows for non-integer values of N_n (Price 2012a). Here we solve the equation for the h_i by requiring an integer value for N_{nn}, to which we will generically refer to in the following as the neighbor number.

Following Price (2012a), the Euler equations are derived using a Lagrangian formulation

$$\frac{d\boldsymbol{v}_i}{dt} = -\sum_j m_j \left[\frac{P_i}{\Omega_i \rho_i^2} \, \boldsymbol{\nabla}_i W_{ij}(h_i) + \frac{P_j}{\Omega_j \rho_j^2} \, \boldsymbol{\nabla}_i W_{ij}(h_j) \right], \quad (3)$$

where Ω_i is defined as

$$\Omega_i = \left[1 - \frac{\partial h_i}{\partial \rho_i} \sum_k m_k \frac{\partial W_{ik}(h_i)}{\partial h_i} \right]. \quad (4)$$

2.2. Artificial Viscosity

The momentum Equation (3) must be generalized to include an artificial viscosity (AV) term, which in SPH represents the effects of shocks. This is introduced in order to prevent particle streaming and to convert kinetic energy into heat at shocks; the new term reads

$$\left(\frac{d\boldsymbol{v}_i}{dt} \right)_{\text{AV}} = -\sum_i m_j \Pi_{ij} \, \boldsymbol{\nabla}_i \bar{W}_{ij}, \quad (5)$$

where $\bar{W}_{ij} = \frac{1}{2}(W(r_{ij}, h_i) + W(r_{ij}, h_j))$ is the symmetrized kernel and Π_{ij} is the AV tensor.

The latter is written following the formulation of Monaghan (1997), based on an analogy with the Riemann problem:

$$\Pi_{ij} = -\frac{\alpha_{ij}}{2} \frac{v_{ij}^{\text{AV}} \mu_{ij}}{\rho_{ij}} f_{ij}, \quad (6)$$

where ρ_{ij} is the average density, $\mu_{ij} = \boldsymbol{v}_{ij} \cdot \boldsymbol{r}_{ij}/|r_{ij}|$ if $\boldsymbol{v}_{ij} \cdot \boldsymbol{r}_{ij} < 0$ but zero otherwise and $\boldsymbol{v}_{ij} = \boldsymbol{v}_i - \boldsymbol{v}_j$. The signal velocity v_{ij}^{AV} is introduced as

$$v_{ij}^{\text{AV}} = c_i + c_j - 3\mu_{ij}, \quad (7)$$

with c_i being the sound velocity. The amount of AV is regulated by the parameter α_i, and f_i is a viscosity limiter, which is introduced so as to suppress AV when strong shear flows are present. This is written as (Balsara 1995)

$$f_i = \frac{|\boldsymbol{\nabla} \cdot \boldsymbol{v}|_i}{|\boldsymbol{\nabla} \cdot \boldsymbol{v}|_i + |\boldsymbol{\nabla} \times \boldsymbol{v}|_i}, \quad (8)$$

where $(\boldsymbol{\nabla} \cdot \boldsymbol{v})_i$ and $(\boldsymbol{\nabla} \times \boldsymbol{v})_i$ are estimated according to the SPH formalism.

The early SPH formulation (Monaghan 2005), assumed a constant viscosity parameter α_i of order unity for all the particles, thus making the scheme excessively viscous away from shocks. In the literature, the SPH scheme with this viscosity parametrization is often referred to as standard SPH, whereas here we use this term to indicate the SPH formulation that uses the AV switch, which now we will describe.

To reduce the amount of AV away from shocks, Morris & Monaghan (1997) proposed letting the α_i's vary with time according to some source term S_i. The time evolution of α_i is given by

$$\frac{d\alpha_i}{dt} = -\frac{\alpha_i - \alpha_{\min}}{\tau_i} + S_i, \quad (9)$$

where $\alpha_{\min}$ is a floor value and

$$\tau_i = \frac{h_i}{c_i \, l_{\text{d}}} \quad (10)$$

is a decay timescale, which is controlled by the dimensionless decay parameter l_{d}. The source term S_i is constructed so that it increases whenever $\boldsymbol{\nabla} \cdot \boldsymbol{v}_i < 0$ (Morris & Monaghan 1997); here we adopt a slightly modified form (Valdarnini 2011), which reads

$$\tilde{S}_i = f_i S_0 \max\left(-(\boldsymbol{\nabla} \cdot \boldsymbol{v})_i, 0 \right)(\alpha_{\max} - \alpha_i)$$
$$\equiv S_i (\alpha_{\max} - \alpha_i),$$

where $\alpha_{\max}$ sets an upper limit and S_0 is unity for $\gamma = 5/3$. In the following, unless otherwise specified, we adopt a time-dependent AV scheme with parameters $\{\alpha_{\min}, \alpha_{\max}, l_{\text{d}}\} = \{0.1, 1.5, 0.2\}$. This set of parameters will be denoted as AV_2 (see Table 1 of Valdarnini 2011, to which we refer for more details).

To suppress AV more efficiently away from shocks, the time-dependent AV scheme has been further improved by Cullen & Dehnen (2010). They introduced the time derivative of $\boldsymbol{\nabla} \cdot \boldsymbol{v}_i$ to detect in advance when a flow is converging, as well as higher order gradient estimators and a more sophisticated functional form for the viscosity limiter in shear flows. The Cullen & Dehnen (2010) scheme will be used in some test cases and we refer to the authors' paper for a detailed description of its implementation in SPH.

2.3. The AC Scheme

In the entropy formulation of SPH, the rate of entropy generation is given by (Springel & Hernquist 2002)

$$\frac{dA_i}{dt} = \frac{\gamma - 1}{\rho_i^{\gamma-1}} \{Q_{\text{AV}} + Q_{\text{AC}}\}, \quad (11)$$

where the terms in brackets denote different sources (in the hydrodynamic test cases presented here, radiative losses are not considered).

The term Q_{AV} refers to the numerical viscosity,

$$Q_{\text{AV}} = \left(\frac{du_i}{dt} \right)_{\text{AV}} = \frac{1}{2} \sum_j m_j \Pi_{ij} \boldsymbol{v}_{ij} \cdot \nabla_i \bar{W}_{ij}. \quad (12)$$

The AC term Q_{AC} for the dissipation of energy takes the form

$$\left(\frac{du_i}{dt} \right)_{\text{AC}} = \sum_j \frac{m_j v_{ij}^{\text{AC}}}{\rho_{ij}} [\alpha_{ij}^C (u_i - u_j)] \boldsymbol{e}_{ij} \cdot \boldsymbol{\nabla}_i \bar{W}_{ij}, \quad (13)$$

where v_{ij}^{AC} is the AC signal velocity, $\boldsymbol{e}_{ij} \equiv \boldsymbol{r}_{ij}/r_{ij}$, and α_i^C is the AC parameter, which is of the order of unity. The above equation represents the SPH analogue of a diffusion equation of the form (Price 2008)

$$\left(\frac{du_i}{dt} \right)_{\text{AC}} \simeq D_i^{\text{AC}} \nabla^2 u_i, \quad (14)$$

where D_i^{AC} is a numerical heat-diffusion coefficient given by

$$D_i^{\text{AC}} \simeq \frac{1}{2} \alpha_i^C v_{ij}^{\text{AC}} r_{ij}. \quad (15)$$

A crucial issue concerns reducing the AC in the absence of contact discontinuities. In analogy with the AV scheme, one can define an AC switch with a source term given by

$$S^C_i = f_C h_i \frac{|\nabla^2 u_i|}{\sqrt{u_i + \varepsilon}} (\alpha^C_{max} - \alpha^C_i), \quad (16)$$

where the Laplacian of the thermal energy is calculated as done by Brookshaw (1985):

$$\nabla^2 u_i = 2 \sum_j m_j \frac{u_i - u_j}{\rho_j} \frac{\boldsymbol{e}_{ij} \cdot \boldsymbol{\nabla} W_{ij}}{r_{ij}}, \quad (17)$$

and for the signal velocity we use (V12)

$$v^{AC}_{ij} = |(\boldsymbol{v}_i - \boldsymbol{v}_j) \cdot \boldsymbol{r}_{ij}|/r_{ij}. \quad (18)$$

For the other parameters, we set $f_C = 1$, $\alpha^C_{min} = 0$, $\alpha^C_{max} = 1.5$, and $\varepsilon = 10^{-4} u_i$.

The time evolution of the AC parameter α^C_i is similar to that of the AV

$$\frac{d\alpha^C_i}{dt} = -\frac{\alpha^C_i - \alpha^C_{min}}{\tau^C_i} + S^C_i, \quad (19)$$

where $\tau^C_i = h_i/0.2c_i$ sets the decaying timescale away from jumps in thermal energy.

The AC term has been introduced with the purpose of smoothing the thermal energy at contact discontinuities (Price 2008), and when using the signal velocity (18) can be interpreted as a subgrid model mimicking the effects of diffusion due to turbulence (Wadsley et al. 2008). Finally, it must be stressed that for the hydrodynamic test problems considered here, with the exception of the KH tests, thermal energy gradients are null or very small. For these tests, the impact of AC on simulation results can then be considered negligible.

2.4. The Integral Approximation (IA) Scheme

In SPH, the errors associated with finite sampling cannot be simply eliminated by a more accurate interpolation scheme. A gradient estimator, which is exact at linear order, can be constructed by using a matrix inversion (Price 2012a), but this comes at the cost of losing the conservation properties of SPH.

To avoid these difficulties García-Senz et al. (2012) proposed a novel approach in which SPH first-order derivatives are estimated through the use of integrals. This makes the method much less noisy than in the standard formulation, with accuracy in estimated gradients being greatly improved (García-Senz et al. 2012; Rosswog 2015).

Moreover, a significant benefit of the method is that it retains the Lagrangian nature of SPH, thereby ensuring exact conservation of linear and angular momentum.

After the paper of García-Senz et al. (2012), the performance of the scheme was investigated in detail by Rosswog (2015); here we briefly describe the essential features of the method.

Let us define the integral

$$I(\boldsymbol{r}) = \int_V [f(\boldsymbol{r}') - f(\boldsymbol{r})](\boldsymbol{r}' - \boldsymbol{r}) W(|\boldsymbol{r}' - \boldsymbol{r}|, h) d^3 r', \quad (20)$$

where W is a spherically symmetric and normalized kernel. By Taylor expanding $f(\boldsymbol{r}')$ to first order around $\boldsymbol{r}$

$$I_\alpha \simeq \boldsymbol{\nabla}_\beta f \int \Delta_\alpha \Delta_\beta W d^3 r', \quad (21)$$

where we have introduced the notation $\Delta_\alpha = (\boldsymbol{r}' - \boldsymbol{r})_\alpha$. The gradient of the function f is then given by

$$\boldsymbol{\nabla}_\alpha f = [\tau]^{-1}_{\alpha\beta} I_\beta, \quad (22)$$

where $\mathcal{T} = \{\tau\}_{\alpha\beta}$ and

$$\tau_{\alpha\beta} = \tau_{\beta\alpha} = \int \Delta_\alpha \Delta_\beta W d^3 r'. \quad (23)$$

SPH integrals are replaced by summations over particles, so that, for the matrix $\mathcal{T}$ of particle i, one has

$$\tau_{\alpha\beta}(i) = \sum_k \frac{m_k}{\rho_k} \Delta^{ki}_\alpha \Delta^{ki}_\beta W(r_{ik}, h_i). \quad (24)$$

In evaluating the discrete equivalent of the integral (20), a key step is to assume that the condition

$$\sum_k \frac{m_k}{\rho_k} (\boldsymbol{r}_k - \boldsymbol{r}_i) W_{ik} \simeq 0 \quad (25)$$

is fulfilled with a certain degree of accuracy. In such a case, the integral (20) then becomes

$$I_\beta(i) = \sum_k \frac{m_k}{\rho_k} f_k \Delta^{ki}_\beta W(r_{ik}, h_i). \quad (26)$$

Because of the approximation (25), for linear functions, -gradient estimates are no longer exact. However, it can easily be seen (García-Senz et al. 2012) that the gradient approximation (22), obtained using Equations (24) and (26), is now antisymmetric in the pair ij. Thus, the condition (25) in the new scheme is crucial for ensuring exact conservation properties.

How well the approximation (25) is valid depends on the particle distribution within the kernel radius. The validity of the new scheme has been carefully tested (García-Senz et al. 2012; Rosswog 2015) for several hydrodynamical problems, demonstrating significant improvements in the accuracy of the results with respect to standard SPH.

To summarize, the IA implies the replacement of $[\boldsymbol{\nabla}_i W_{ik}]_\alpha$ in the SPH equations according to the following prescriptions:

$$[\nabla_i W_{ik}(h_i)]_\alpha \rightarrow \sum_\beta C_{\alpha\beta}(i) \Delta^{ki}_\beta W(r_{ik}, h_i) \quad (27)$$

and

$$[\nabla_i W_{ik}(h_k)]_\alpha \rightarrow \sum_\beta C_{\alpha\beta}(k) \Delta^{ki}_\beta W(r_{ik}, h_k), \quad (28)$$

where $\mathcal{C} = \mathcal{T}^{-1}$. In the following, the SPH formulation in which gradients are estimated according to the numerical scheme described here, will be referred to as the IA.

3. KERNELS

In this section, we briefly review some properties of the most commonly used kernels in SPH. All of these kernels are characterized by the property of having compact support and of being continuous up to some degree.

A class of kernels that has often been considered in SPH is that of the B-spline functions (Price 2012a), which are generated via the one-dimensional (1D) Fourier transform:

$$M_n(x, h) = \frac{1}{2\pi} \int_{-\infty}^{\infty} \left[\frac{\sin(kh/2)}{kh/2} \right]^n \cos(kx) dk. \quad (29)$$

The degree of smoothness increases with n and the kernel approaches the Gaussian in the limit $n \rightarrow \infty$. The function M_n

is a polynomial of degree $n - 1$ and its derivative is continuously differentiable $n - 2$ times. By requiring in SPH the continuity of the first and second derivative, the first useful kernel is then M_4 (cubic spline):

$$w(q) = \frac{\sigma}{h^D} \begin{cases} \frac{1}{4}(2 - q)^3 - (1 - q)^3 & 0 \leqslant q < 1, \\ \frac{1}{4}(2 - q)^3 & 1 \leqslant q < 2, \\ 0. & q \geqslant 2, \end{cases} \quad (30)$$

where the kernel is non-zero for $0 \leqslant q \leqslant \zeta = 2$ and ζ is the truncation radius in units of h_i. The normalization constant takes the values $\sigma = 10/7\pi$, $1/\pi$ for $D = 2$ and $D = 3$, respectively.

The B-splines in the order in which have been considered are M_5 ($\zeta = 2.5$) and M_6 ($\zeta = 3$); for a more detailed description of these kernels, we refer the reader to Price (2012a).

The stability properties of the M_n kernel family have been investigated by a number of authors (Morris 1996; Børve et al. 2004; Read et al. 2010; Dehnen & Aly 2012, V12). A crucial result, which emerges from these analyses, is that all of the B-splines suffer from pairing instability. The number of neighboring particles for which the instability develops depends on the kernel degree and in 3D lies in the range between $N_n \simeq 50$ for M_4 up to $N_n \simeq 200$ when the M_6 kernel is used (Dehnen & Aly 2012).

It has been suggested that particle clumping can be avoided by modifying the kernel shape in order to have a non-zero gradient at the origin. Examples of this family of kernels are the core-triangle (Read et al. 2010) and the linear quartic (LIQ; Valcke et al. 2010). However, such adjustments reflect negatively on the density estimation ability of the kernels. By introducing a non-zero central derivative, the kernel profile becomes steeper and this in turn implies an overestimate of density when compared with the corresponding B-spline (V12, Rosswog 2015).

These attempts to fix the pairing instability by introducing ad hoc modifications in the kernel shape have recently been superseeded by a new class of kernels. It has been shown (Dehnen & Aly 2012) that a necessary condition for avoiding pairing instability is that of having kernels with non-negative Fourier transforms. A class of kernels that satisfies this property and has compact support are the Wendland (1995) functions. An example in 3D of these functions is the Wendland C^4:

$$w(q) = \frac{495}{32\pi}(1 - q)^6 \left(1 + 6q + \frac{35}{3}q^2\right), \quad (31)$$

where $w(q) = 0$ if $q > 1$. Hereafter, we will refer to this kernel as $W4$. Other classes of Wendland kernels are C^2 ($W2$) and C^6 ($W6$). We refer to Table 1 of Dehnen & Aly (2012) for the functional forms and normalization of these kernels. Finally, García-Senz et al. (2014) proposed using the sinc functions as another class of kernels which can be used to avoid pairing instability.

The accuracy of density estimation in SPH for different kernel families has been assessed by many authors (Dehnen & Aly 2012; V12; Rosswog 2015; Zhu et al. 2015). Here we measure the mean SPH density of $N = 128^3$ particles using a glass-like particle distribution inside a cube of sidelength unity and total mass one. Figure 1 shows the mean SPH density of
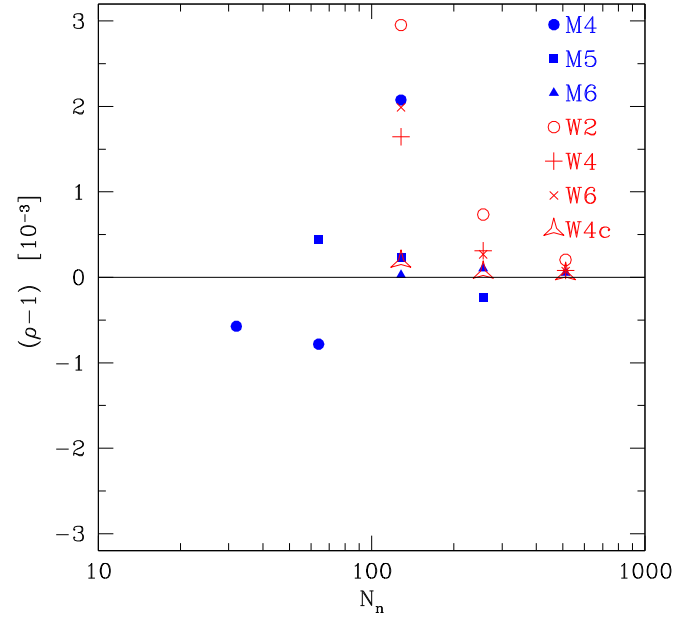

Figure 1. Average SPH density calculated for a glass-like configuration of 128^3 particles in a periodic box of unit length. The theoretical expected value is $\rho = 1$ and the quantity plotted is $(\rho - 1)/10^{-3}$. Different symbols refer to different kernels; for the sake of clarity, error bars are not shown. The symbol $W4c$ refers the Wendland kernel $W4$, but with the self-correction term of Dehnen & Aly (2012, Equation (18)) included.

the particles as a function of the neighbor number N_n for different B-splines and Wendland kernels. The value of N_n ranges in powers of two between $N_n = 32$ and $N_n = 512$, with three distinct values of N_n being considered for each kernel according to its order (see Figure 1). To avoid overcrowding in the plot, standard deviation σ's are not shown, but the general tendency is of σ decreasing as N_n increases with $\sigma \simeq 10^{-3}$ for the largest value of N_n.

A number of conclusions can be drawn by examining, for different kernels, the accuracy behavior depicted in Figure 1. The best performances are given by M_5 and M_6, which for any given number of neighbors N_n outperform all of the other kernels. The cubic spline (M_4) and the Wendland $C2$ ($W2$) exhibit the worst performances, regardless of the value of N_n.

The Wendland kernels yield acceptable density estimates only when large values of N_n are used ($N_n \gtrsim 250$), with M_5 and M_6 having better performances at any given N_n and stable estimates already for $N_n = 128$. The differences between the two families reduce progressively as N_n is increased, with the results becoming comparable only when $N_n = 512$.

This behavior reflects the difference in shape between the two families, with the Wendland kernels being more centrally peaked than the B-splines and systematically overestimating the density. This, in turn, is a direct consequence of the way in which the Wendland kernels have been constructed in order to avoid pairing instability and of their spectral properties.

It must be stressed that in making comparisons between the error behavior of kernels of different families, it is only meaningful to compare kernels with the same polynomial order (Aguilar et al. 2011). In 3D, the Wendland equivalent of the M_6 kernel is therefore $W2$.

This means that, in relative terms, the performances of the Wendland kernels are not very good unless one is willing to use a very large number of neighbors in the SPH simulations

made with them. In this respect, it is now common practice to use the Wendland kernels $W4$ (or even $W6$) setting $N_n \simeq 200$. However, even small errors in the densities can have a significant impact on estimates of other hydrodynamic variables (see the results for the Sod shock tube in V12). Thus, in the case of using Wendland kernels, a conservative lower limit on the neighbor number to be used in 3D SPH runs should be $N_n \simeq 400$.

To improve the performances of Wendland kernels, Dehnen & Aly (2012, see their Equation (18)) proposed the subtraction of a fraction of the particle i self-contribution from the SPH density estimate (1). The correction term depends on the kernel order and neighbor number, with an impact that decreases as one of the two increases. For the Wendland kernel $W4$, in Figure 1, we show density estimated using the self-correction term ($W4c$), which now brings the relative density error down to $\sim 10^{-4}$.

However, for the hydrodynamic tests presented here, the numerical set-ups consist of particle positions arranged in lattice- or glass-like configurations with densities of the order of unity. This suggests that one can use the results of Figure 1 to assess density errors, which are already very small ($\sim 10^{-3}$) without the use of such a correction term. Therefore, for the considered runs, we expect a negligible impact of the self-correction term on SPH densities, and it will not be considered in what follows.

These results hold for a glass-like configuration, but it is difficult to assess the error behavior for a realistic SPH distribution of particles. Zhu et al. (2015) put the expected convergence rate between that found for a random distribution set ($\sigma \propto N_n^{-0.5}$) and the one measured for a highly ordered distribution ($\sigma \propto N_n^{-1}$), such as a glass-like configuration. These findings strengthen the previous conclusions, suggesting that when using Wendland kernels in SPH, the number of neighbors should be kept as high as possible.

4. HYDRODYNAMIC TESTS

In the following, we analyze results from some test problems aimed at assessing code performance of the new IA scheme. As already outlined in the Introduction, the problems considered here have been chosen with the specific aim of investigating code behavior when subsonic flows are present in the hydrodynamic tests.

This is motivated by the serious shortcomings that affect standard SPH in these regimes. We first discuss the Gresho–Chan test, which, in this respect, presents severe challenges to the SPH scheme, and then the others.

4.1. The Gresho–Chan Vortex Problem

The Gresho–Chan (Gresho & Chan 1990) vortex consists of a fluid of uniform density in differential rotation, with centrifugal forces balancing pressure gradients. The system is stationary and any change in the azimuthal velocity profile that arises during the integration is then due to numerical artifacts.

Because of sampling effects, errors in force accuracy lead to noise in the velocity field, thus generating numerical viscosity and hence particle disorder due to the spurious transport of angular momentum. It is then particularly problematic for standard SPH to successfully model this problem leaving unaltered the velocity profile during the simulation, and in the literature (Springel 2010; Dehnen & Aly 2012; Read &

Hayfield 2012; Kawata et al. 2013; Hu et al. 2014; Hopkins 2015; Rosswog 2015; Zhu et al. 2015) it has been widely used to validate code performances.

We next describe our initial condition's setup. We take a gas with a uniform density of $\rho = 1$ within the periodic domain $0 \leqslant x, y < 1$, with zero radial velocity, azimuthal velocity profile

$$v_\phi(r) = \begin{cases} 5r & (0 \leqslant r \leqslant 0.2) \\ 2 - 5r & (0.2 < r \leqslant 0.4) \\ 0 & (r > 0.4), \end{cases} \quad (32)$$

and pressure profile

$$P(r) = P_0 + \begin{cases} 12.5r^2 & (0 \leqslant r \leqslant 0.2) \\ 12.5r^2 - 20r + \\ 4 + 4\ln(5r) & (0.2 < r \leqslant 0.4) \\ 2(2\ln 2 - 1) & (r > 0.4), \end{cases} \quad (33)$$

where $r = \sqrt{x^2 + y^2}$, $P_0 = (\gamma M^2)^{-1}$, $\gamma = 5/3$ and M is the Mach number. Here we have adopted the generalized expression for the background pressure of Miczek et al. (2015), so that we can consider subsonic shear flows with low Mach numbers (Hu et al. 2014). The standard Gresho case is recovered for $M = \sqrt{3/25} \simeq 0.34$, giving $P_0 = 5$.

Particle positions are initialized using an $N \times N \times 16$ lattice of particles (Zhu et al. 2015), N being the effective 1D resolution. For the box thickness, we set $L_z = 16/N$ and we always consider $N > 32$. Here we use a hexagonal-close-packed (HCP) configuration for the particle coordinates. The particle velocities and pressure are set according to Equations (32) and (33). All of the simulations are run up to a final time $t_f \simeq 3M$, using a fixed timestep $\Delta t = t_f/(800 \cdot 64)$, so as to ensure the same integration accuracy in runs with different Mach numbers.

We quantify the convergence rate for different runs by using the $L1$ error norm for the velocity (Springel 2010)

$$L1(v_\phi) = \frac{1}{N_b} \sum_i^{N_b} |\bar{v}_\phi(i) - v_\phi(r_i)|, \quad (34)$$

where the summations is over N_b bins, we set a binsize of $\Delta = 0.01$ in the range of $0 \leqslant R \leqslant 0.5$ (Hu et al. 2014), $\bar{v}_\phi(i)$ is the average azimuthal velocity of the particles, which lie in the ith bin interval, and $v_\phi(r_i)$ is the analytic solution at the bin radial coordinate.

Figure 2 shows the azimuthal velocity profiles for $M = 0.34$ at $t = 1$; the one-dimensional resolution is $N = 128$ and each panel refers to a different kernel. Within each panel, lines with different color codes are for different neighbor numbers, and the standard run always refers to the lowest neighbor number indicated in the panel. In this case, for the B-splines, values of N_n are considered, which are below the pairing instability threshold.

It is clear from all of the histograms that the IA scheme outperforms the standard one for all of the kernels, with the latter scheme being much more noisy. There is a tendency for the standard scheme to improve as higher order kernels are considered, but the error in the velocity profile is always significant. These results are in agreement with previous findings (Dehnen & Aly 2012; Read & Hayfield 2012; Hu et al. 2014; Rosswog 2015) and clearly demonstrate how, for the vortex test, inaccuracies in gradient estimates, i.e., the E_0
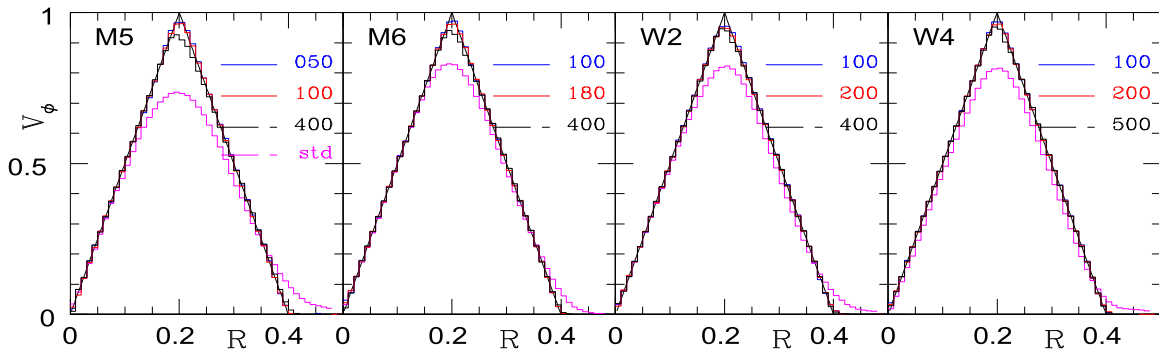
Figure 2. Azimuthal velocity profile of the Gresho–Chan vortex test for $M = 0.34$ at $t = 1$, with 1D resolution $N = 128$. Each panel is for a different kernel and, in each of them, lines of different color are for different neighbor number. For a given kernel in the standard run, the lowest neighbor number is used.

error, are the leading error sources. These errors are significantly reduced when using the IA scheme, showing how good that method is.

To quantify the performance of the IA approach, for the same test case, we show at $t = 1$ the velocity error $L1$ as a function of the 1D resolution N in Figure 3. This ranges between $N = 50$ up to a maximum value of $N = 500$. For any given value of N, we considered different combinations of kernel and neighbor number N_n; these are reported in the figure. For the same combination of resolution, kernel shape, and neighbor number, we performed a simulation according to the IA formulation and a corresponding one using standard SPH.

In the case of the B-splines, we employed the highest neighbor number that it is possible to use without having the pairing instability. For the Gresho–Chan vortex test, the convergence rate has already been estimated for a variety of different SPH implementations, so that Figure 3 can be compared with the corresponding rates already obtained by various authors (Dehnen & Aly 2012; Read & Hayfield 2012; Hu et al. 2014; Rosswog 2015; Zhu et al. 2015).

From Figure 3, it can be seen that there is a resolution dependency of the $L1$ error on N. In the standard case, the convergence behavior is in line with those found previously, see for example Figure 10 of Dehnen & Aly (2012) or Figure 5 of Zhu et al. (2015). The dependency of $M5$ on resolution parallels that of the $W2$ kernel and the same holds for the kernels $M6/W4$, this is very similar to what is seen in Figure 10 of Dehnen & Aly (2012, we use the same neighbor number). However, for the $L1$ norm, we obtained smaller errors here. For example, in the $M6/W4$ case, we found that for $N = 400$ $L1 \simeq 7 \times 10^{-3}$, whereas for the same test run their Figure 10 shows $L1 \simeq 0.015$. The same is true for the $W6$ runs, for which here $L1(N = 400) \simeq 3 \times 10^{-3}$ is about a factor three smaller than in their corresponding run.

When passing from the standard scheme to the IA scheme, there is a significant reduction in the amplitude of the $L1$ norms. The decrease in $L1$ is by a factor of between ~ 5 and ~ 10, with some dependency on resolution and adopted kernels. For the $M5$ ($N_n = 60$) kernel, the ratio between the norms ranges from $L1(IA)/L1(std) \simeq 1/8$ at $N = 50$ down to $\sim 1/30$ when $N_n = 500$.

We now analyze the convergence rate of $L1$ in the IA formulation. This depends on the adopted kernel, and for $M5$ we found $L1 \propto N^{-1.2}$. This is close to what was given by Springel (2010) when using the moving-mesh code Arepo ($L1 \propto N^{-1.4}$).
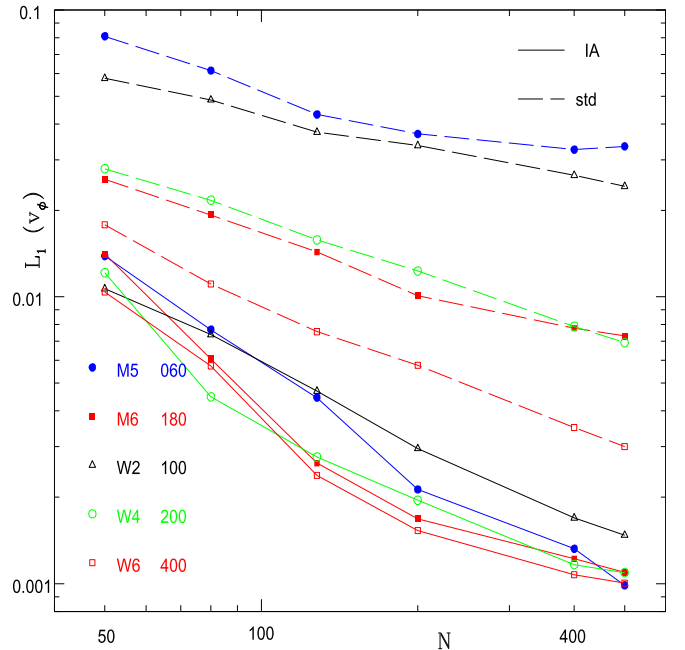

Figure 3. Convergence rate of the $L1$ velocity error for the Gresho–Chan vortex test. The $L1$ error is shown vs. the 1D particle number for $M = 0.34$ at $t = 1$. Dashed lines are for the standard formulation and solid lines refer to the IA scheme. The symbols indicate different combinations of kernel and neighbor number.

To estimate the rate for the other kernels, we adopt a conservative view and only include in the fit those points with $N \geqslant 80$. We then obtain $L1 \propto N^{-1}$, which is better than that reported by Hu et al. (2014, $L1 \propto N^{-0.7}$) for their pressure-entropy SPH formulation. The rate is also in agreement with that shown by Rosswog (2015, Figure 10, case $F3$: $L1 \propto N^{-1}$), who implemented an IA scheme using a $W6$ kernel. Note, however, that the value of $L1$ at $N = 300$ found there is a factor of approximately three higher than that found here ($L1 \sim 10^{-3}$).

Higher convergence rates have been obtained by Read & Hayfield (2012, $L1 \propto N^{-1.4}$), who employed a modified version of SPH with high-order dissipation switches, and by Zhu et al. (2015). The latter investigated the convergence behavior of standard SPH, showing that consistency in numerical convergence is achieved when the conditions $N \to \infty$ $h \to 0$ $N_n \to \infty$ are satisfied. In their varying N_n case ($N_n = 120 \cdot (N/32)^{1.2}$), for the Gresho–Chan vortex test, the
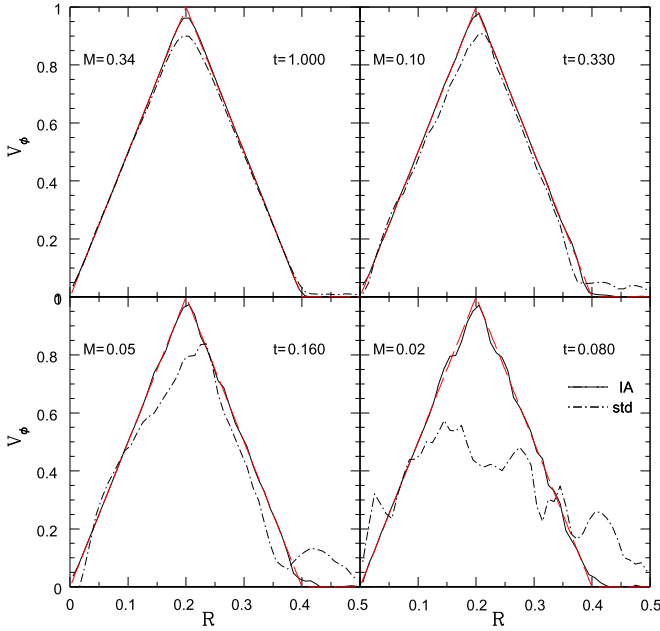
Figure 4. Velocity profiles of the Gresho–Chan vortex test for $M = 0.34, 0.1, 0.02, 0.05$ (clockwise from top-left) at the final times $t_f \simeq 3M$. The tests have been performed using $N = 128$ and the $M6$ kernel with $N_n = 180$ neighbors. Solid lines are for the IA formulation, dotted–dashed lines refer to the standard scheme. The dashed line in color is the analytical solution. The figure can be compared with Figure 2 of Hu et al. (2014).

authors report $L1 \propto N^{-1.2}$, a much faster rate than that obtained by keeping N_n constant. The value of $L1$ in the $N = 500$ case is of the same order ($L1 \simeq 3 \times 10^{-3}$) as that obtained here for the $W6$ standard run with the same resolution.

Finally, with the exception of the lowest order kernels ($M5$ and $W2$), a comparison of the $L1$ norms with those produced using the moving-mesh code Arepo shows that the IA formulation gives results that are comparable or better than those obtained with the mesh code (Springel 2010, Figure 29), with $L1$ ranging here from $L1 \simeq 8 \times 10^{-3}$ ($N = 80$) down to $L1 \simeq 10^{-3}$ ($N = 500$).

To further investigate the performance of the IA scheme, we ran a suite of vortex tests with progressively lower Mach numbers. These tests are particularly challenging since, at constant velocity, the lower is the Mach number and the higher is the sound speed. This in turn implies an increase in the viscous force. Errors in the momentum equation then become progressively more important.

To aid comparison with the previous works, as in Hu et al. (2014) we considered the following Mach numbers $M = 0.02, 0.05, 0.1,$ and $M = 0.34$. We ran the simulations using $N = 128$ as 1D resolution. This is a factor of two lower than that used by Hu et al. (2014) in their tests; however, the results are not significantly affected by this choice. For the $M6$ kernel ($N_n = 180$), we show the azimuthal velocity profiles of the four test cases in Figure 4, so that the figure can be compared with the corresponding histograms of Figure 2 of Hu et al. (2014).

The profiles of the standard runs largely reproduce those of Hu et al. (2014); however, a striking feature of the IA scheme, which emerges from the histograms of Figure 4, is the close proximity of the azimuthal velocity profiles to the analytical solution. This occurs even when very low Mach numbers are considered, as can be seen from the $M = 0.02$ case. This shows

the effectiveness of the IA method for eliminating sampling errors in SPH when subsonic flows are present.

Moreover, these findings are in agreement with previous results (Read & Hayfield 2012; Hu et al. 2014) and demonstrate that in SPH simulations of the Gresho–Chan test, errors in force accuracy dominate over viscous effects.

For the considered tests, we have shown until now the mean binned velocities. In order to assess the amount of noise present in the various runs, it is useful to directly plot the azimuthal particle velocities. To this end, we ran two tests with 1D resolution $N = 128$, Mach numbers $M = 0.34$, and $M = 0.06$, respectively. In the latter case, we set a background pressure of $P_0 = 50$. For each run performed using the time-dependent AV scheme with settings AV_2 (see Section 2.2), we also consider a parent simulation in which the AV switch of Cullen & Dehnen (2010) has been implemented.

The results are shown in Figure 5 at $t = 3$, where for the two test cases we plot the azimuthal velocities for a subset of all particles. The velocity distributions can be compared directly with those of the corresponding runs in Figures 4 and 5 of Hopkins (2015). An important feature that emerges from the plots of Figure 5 is that both AV methods show velocity distributions that are evenly scattered around the analytic solution, with the AV switch of Cullen & Dehnen (2010) exhibiting a much smaller amount of noise. It is worth noting how the IA method, even for very low Mach numbers, can accurately follow the analytic solution also at the peak vortex velocity. This behavior is much better than that seen for the same test in the top panel of Figure 5 of Hopkins (2015).

Finally, it must be pointed out that the amount of thermal diffusion due to the AC term is negligible in these simulations and we do not include such a term in the SPH equations. This occurs because of the high sound speeds in the low Mach number regime, so that the time evolution (19) of the α_i^C parameter is driven by the decaying rate $1/\tau_i^C$, which dominates over the source term S_i^C. To better quantify this issue, we use Equation (14) to estimate at time t the change in thermal energy due to the AC term: $\Delta u_{AC} \simeq t(D^{AC}\nabla^2 u)$.

The Laplacian of u has a maximum at $r = 0.2$, where the azimuthal velocity reaches its peak value. The diffusion coefficient is then given by $D_i^{AC} \simeq \alpha_i^C 5 r_{ij} r_{ij}/2 \simeq 5\alpha_i^C h_i^2/2$, so that

$$\Delta u_{AC} \simeq \frac{5}{2}\alpha_i^C h_i^2 \nabla^2 u_i t = \frac{5}{2}(S_i^C \tau_i^C)h_i^2 \nabla^2 u_i t, \qquad (35)$$

where we have approximated α_i^C with the equilibrium solution $\alpha_i^C(eq) \simeq S_i^C \tau_i^C \simeq h_i^2 \nabla^2 u_i/(0.2 c_i \sqrt{u_i})$.

For $M = 0.34$ at $r = 0.2$ $u \sim 15/2$, $\nabla^2 u \sim 300/4$, $c_i \sim 3$ and h_i can be easily computed because $\rho = 1$ so that

$$\Delta u_{AC} \simeq 8.6 \times 10^3 h_i^4 t. \qquad (36)$$

For $N \gtrsim 50$ and $t \lesssim 3$, this term is always much smaller than u, regardless of the chosen kernel.

4.2. The KH Instability

The KH instability has been investigated by many authors since it is a classic test in which SPH fails to properly model the development of the instability (Price 2008; Cha et al. 2010; Heß & Springel 2010; Junk et al. 2010; Read et al. 2010; Valcke et al. 2010; Murante et al. 2011; McNally et al. 2012; Valdarnini 2012; Kawata et al. 2013; Hu et al. 2014; Hopkins 2015).
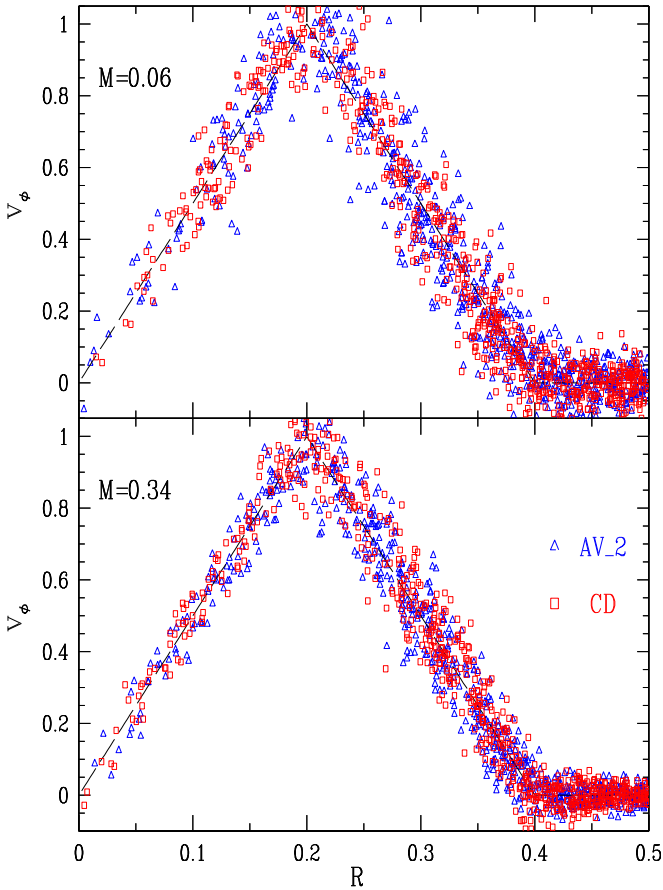
Figure 5. Plots at $t = 3$ of the azimuthal particle velocities for two Gresho–Chan vortex tests, both performed using a one-dimensional resolution of $N = 128$ and the $M6$ kernel with $N_n = 180$ neighbors. The bottom panel is for $M = 0.34$ and the top panel for $M = 0.06$ with $P_0 = 50$. The two plots can be compared with the corresponding ones in Figures 4 and 5 of Hopkins (2015). For the sake of clarity, we show velocities of a subset of randomly selected particles. Open triangles are for the time-dependent AV scheme with settings AV_2 (See Section 2.2), open squares refer to the AV switch of Cullen & Dehnen (2010).

The test consists of two fluid layers of different densities sliding past each other with opposite shearing velocities, and a small velocity perturbation is imposed in the direction perpendicular to the contact surface. A fluid instability develops, which is initially small and then becomes progressively larger until nonlinearity is reached with the appearance of KH rolls. For a sinusoidal perturbation of wavelength λ, a linear timescale can be defined as

$$\tau_{KH} = \frac{\lambda(\rho_1 + \rho_2)}{(\rho_1\rho_2)^{1/2}v} \quad, \tag{37}$$

where ρ_1 and ρ_2 are the two fluid densities with a density ratio of $\chi = \rho_1/\rho_2$ and $v = v_1 - v_2$ is the relative shear velocity.

To perform the test, the following conditions

$$\rho, \quad T, v_x \begin{cases} \rho_1, T_1, v_1 & |y - 0.5| \leqslant 0.25 \\ \rho_2, T_2, v_2 & |y - 0.5| > 0.25 \end{cases} \tag{38}$$

are applied for a fluid with adiabatic index $\gamma = 5/3$ in a two-dimensional periodic domain with cartesian coordinates $x \in \{0, 1\}$, $y \in \{0, 1\}$. We set here $\rho_2 = 1$, and $\chi = 2$ for the density contrast.

The two layers are in pressure equilibrium with $P_1 = P_2 = 5/2$, so that the sound velocities in the two layers are $c_2 = \sqrt{\gamma P_2/\rho_2} = 2.04$ and $c_1 = c_2/\sqrt{\chi} = 1.44$, respectively. The Mach number of the high-density layer is $M \simeq v_1/c_1 \simeq 0.7v_1$ and the KH timescale is $\tau_{KH} \simeq 0.177/v_1$. We ran KH simulations with three different Mach numbers: $M = 0.05, \ 0.1$ and $M = 0.35$. For the latter value, the initial condition setup was similar to that of Hopkins (2015, Section 4.4.1).

The KH instability is triggered by adding in the proximity of the layer boundaries a small single-mode velocity perturbation along the y-direction

$$v_y = \delta v_y^{(0)}\sin(2\pi x/\lambda), \tag{39}$$

where $\delta v_y^{(0)} = 2 \times 10^{-2}v_1$, $\lambda = 1/6$, and $v_y = 0$ if $|y - \sigma| > 0.025$, where σ takes the values 0.25 and 0.75, respectively. Note that for the amplitude of the initial velocity perturbation $\delta v_y^{(0)}$ we set here, unlike in previous runs (V12), a relative constant amplitude with respect to the streaming velocity. This was done in order to consistently compare, between runs with different Mach numbers, the impact of zeroth-order errors on $v_y \propto M$.

We performed the initial condition setup by arranging $N^2 = 512^2$ equal mass particles inside the simulation box, setting the particle coordinates according to an HCP configuration. The lattice spacing was smoothly adjusted at the fluid interfaces so as to avoid density discontinuities; the details of the whole procedure are given in V12. For each test case, the IA simulations were then performed using the M_5, $W2$, and the $W4$ kernels with neighbor numbers $N_n = 50$, $N_n = 72$, and $N_n = 162$, respectively. For the $M5$ runs, we also considered standard simulations. Finally, all of the simulations were performed with the AC term of Section 2.3 switched on.

For the specified range of Mach numbers, we first show, in Figure 6, density plots of the KH simulations at $t = \tau_{KH}$. We show maps extracted from the $M5$ runs, and contrast the IA scheme against the standard SPH scheme. For $M = 0.35$, both of the methods are able to produce KH rolls. At lower Mach numbers ($M = 0.1$), the standard method completely fails the KH test, whereas the IA scheme shows a degraded capability to resolve KH rolls. At $M = 0.05$, the rolls are absent and the differences between the two schemes are no longer present.

The relative performances of the two methods can be quantitatively assessed by measuring the E_0 error (Read et al. 2010; Valcke et al. 2010, V12) for the various runs. Here we first show the growth rate of the KH instability (Heß & Springel 2010; Junk et al. 2010, V12), which allows one to recognize the differences between the KH results produced by the two schemes in a more visual way. The growth rate is measured by Fourier transforming, at different times, the $\lambda = 1/6$ growing mode of the v_y velocity perturbation (Junk et al. 2010, V12).

The growth rates are shown in Figure 7, and their relative differences confirm the visual impressions derived from the maps of Figure 6. For $M = 0.35$, there are no significant differences between the two methods and both are able to follow the growth of the KH instability (Figure 6, right panel), the rates of the different runs being in accordance with the analytic expectation. The results can also be compared with the corresponding rates in Figure 18 of Hopkins (2015), taking care to address the different timescales due to the different number
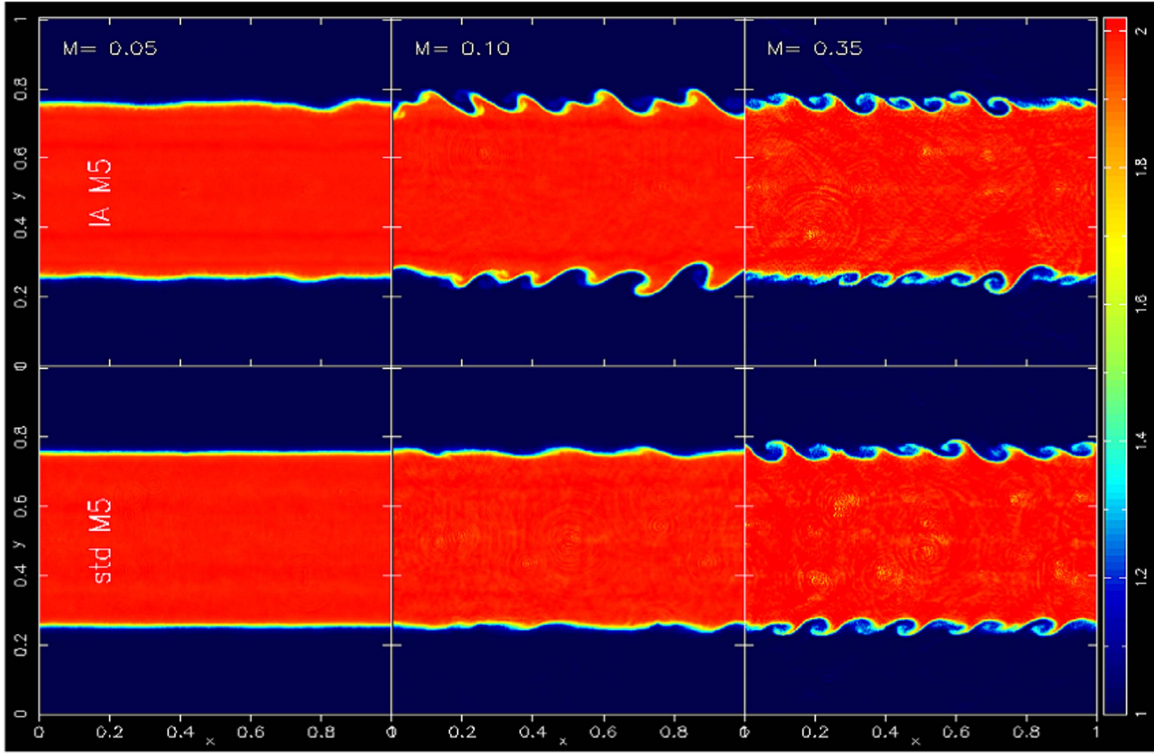
Figure 6. Density maps at $t = \tau_{KH}$ for the 2D KH instability tests described in Section 4.2. The tests have been performed with a density contrast of $\chi = 2$ between the two contact layers. From left to right, the different panels are for different Mach numbers: $M = 0.05$, $M = 0.1$, and $M = 0.35$. Each test case was run separately with both the standard (bottom) and the IA (top) scheme. All of the maps have been extracted from simulations performed using the $M5$ kernel.

of modes used to seed the perturbation. Note that, unlike in Hopkins (2015), the standard version here correctly follows the development of the KH instability. We interpret this difference as being due to the small neighbor number ($\sim$32 in 3D) adopted in his standard (PSPH) run.

As lower Mach numbers are considered, from the other panels of Figure 7 one can see a growing difficulty of the IA scheme in following the KH instability, regardless of the kernel employed in the simulation. This happens because, by reducing the Mach number, the shear velocity is also reduced and in turn, owing to the chosen settings, the initial velocity amplitude is reduced as well. At a fixed resolution, the impact of gradient errors, and the subsequent particle disorder, on the growth of the KH instability is then higher as the Mach number decreases.

The E_0 error of particle i is defined by (Read et al. 2010)

$$E_i^0 = \sum_j \frac{m_j}{\rho_j} \left[\frac{\rho_i}{\rho_j} + \frac{\rho_j}{\rho_i} \right] h_i \, \boldsymbol{\nabla}_i \bar{W}_{ij}, \qquad (40)$$

and we show in Figure 8 the mean binned distribution of the particle errors versus y. The plots refer to the runs of Figure 6. A key feature is the magnitude of the errors, which in proximity of the interfaces for the IA runs are smaller than the standard ones by a factor of approximately five. This is in line with what is expected and is in accordance with what is seen in Figure 7, with the growth rates of the IA runs exhibiting a better behavior at low M. However, one can see from Figure 7 that, for $M = 0.05$, the KH instability is not correctly reproduced even in the IA scheme. In such a case, gradient errors can be reduced by increasing the simulation resolution.

We do not undertake here a resolution study aimed at assessing the convergence rate to the KH solution in the very low ($M \lesssim 0.1$) subsonic regime. We use instead a simple argument to provide a rough estimate of the minimum number of particles N^2, which would be necessary to simulate the $M = 0.05$ KH test case.

An $L1$ error norm for the KH problem has been introduced by Robertson et al. (2010) and, in analogy with their Equation (11), we conjecture here for $L1$ a generic dependence of the form

$$L1 \propto N^{-2\alpha} (1 + t)^{\gamma(N)}, \qquad (41)$$

on the particle number $N_p = N^2$, and the simulation time t. We have dropped the dependency on the bulk flow velocity, present in their Equation (11), and for the power-law dependencies we generically assume the exponents α and $\gamma(N)$.

The simulations of Robertson et al. (2010) were performed using the Eulerian mesh code ART (Kravtsov et al. 1997); note however that their initial condition setup corresponds to the $M = 0.35$ KH test case here.

The ratio between the error norms of two different KH runs is then

$$L_2/L_1 = (N_1/N_2)^{2\alpha} (1 + t_2)^{\gamma_2}/(1 + t_1)^{\gamma_1}, \qquad (42)$$

where we set $t = \tau_{KH} \simeq 0.124/M$ in order to consistently compare the norms and $\gamma_i \equiv \gamma(N_i)$. We now assume as a reference run the $M = 0.35 = M_1$ test case, for which $N = 512$ from Figure 7 can be considered an adequate resolution up to $t = t_1 \sim 0.35$. Therefore, for
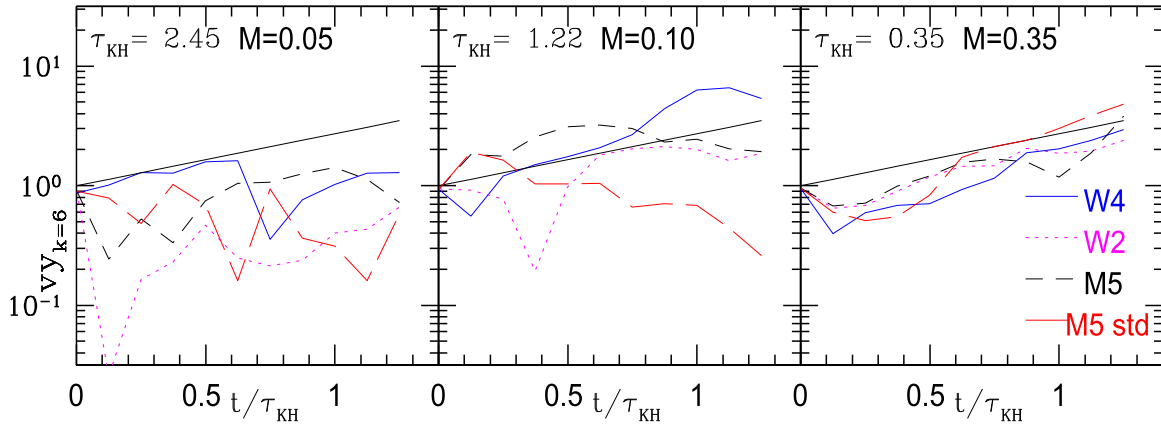
Figure 7. Growth rate of the $\lambda = 1/6$ velocity amplitude as measured by making a Fourier transform of v_y. The KH tests are for a density contrast $\chi = 2$ and three different values of Mach number have been considered ($M = 0.05, 0.1, 0.35$). For each KH test case, we ran IA simulations using the M_5, $W2$, and the $W4$ kernels. Additionally, for the M_5 runs, we also performed a corresponding standard simulation. The solid line is the linear theory growth rate expectation $\propto e^{t/\tau_{KH}}$, normalized to the numerical amplitude at $t = 0$.
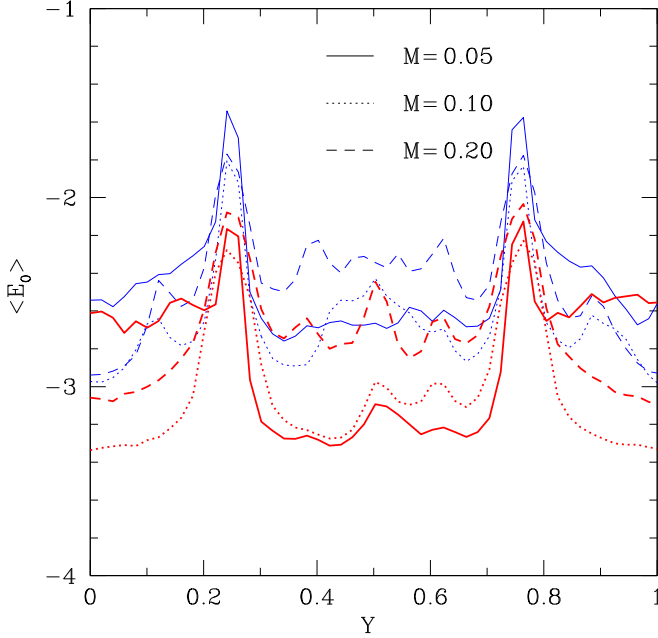

Figure 8. Averaged binned distribution of the particle errors $|E_i^0|$ vs. y for the KH runs of Figure 6. Different lines are for different Mach numbers. Thick red (thin blue) lines refer to IA (standard) runs.

$M_2 = 0.05 = M_1/7$, the norm ratio is

$$L_2/L_1 = (512/N_2)^{2\alpha} (3.45)^{\gamma_2}/(1.35)^{\gamma_1}. \quad (43)$$

For the dependency on simulation resolution, Robertson et al. (2010) report $\alpha = 1$ for their Eulerian code. Here the numerical convergence is likely to be shallower, with $\alpha < 1$. However, the results of Section. 4.1 indicate, for the vortex test, a convergence rate of the IA scheme very close to that seen using moving-mesh schemes (Springel 2010). We therefore assume here $\alpha = 1$ as a reasonable slope on resolution convergence, thus putting a conservative lower limit on N_2.

In Robertson et al. (2010), the time evolution of the error norm has a weak dependency on numerical resolution: $\gamma(N) \simeq 2(64/N)^{0.5}$. This slope clearly depends on the adopted numerical scheme and we simplify this dependency by assuming $\gamma_i = 1$. The impact of this assumption on estimating

N_2 is, however, relatively unimportant, with the ratio between the two time factors being in any case of the order of unity and closer to one as $\gamma_i < 1$. In fact, we further simplify the ratio (43) by just removing the time factors.

Finally, an accuracy criterion for the simulations is set by putting an upper limit on the error norm $L1 \lesssim \text{err}(L1)$, with $\text{err}(L1)$ being a given threshold. We now assume for $\text{err}(L1)$ a generic dependence on the initial velocity amplitude $\delta v_y^{(0)}$ of the form $\text{err}(L1) \propto (\delta v_y^{(0)})^\beta$, with $\beta \geqslant 1$. This lower limit on β is justified by the requirement that lower values of $\delta v_y^{(0)}$ must correspond to lower values of $\text{err}(L1)$. Then, for the ratio (43), we have

$$L_2/L_1 = (512/N_2)^2 \lesssim \left(\frac{\delta v_y^{(0)}(2)}{\delta v_y^{(0)}(1)} \right)^\beta$$

$$= (M_2/M_1)^\beta = (1/7)^\beta.$$

Setting $\beta = 1$, we thus obtain for N_2 the lower limit $N_2 \gtrsim 1500$. Note, however, that to achieve numerical convergence in a consistent way in SPH the number of neighbors N_n must also increase when $N \to \infty$ and $h \to 0$ (Zhu et al. 2015). For their Gresho–Chan vortex test, Zhu et al. (2015) adopt, when N_n is allowed to vary, $N_n \propto N_p^{1.2}$. In such a case, by referring to the $M = 0.35$ $W4$ run with $N_n = 162$ neighbors, we conclude that $N_n \gtrsim 7 \cdot 162 = 1134$ neighbors and $N_p \simeq 2 \times 10^6$ particles are the least necessary in order to simulate the $M = 0.05$ KH test case using the $W4$ Wendland kernel.

Finally, it is worth noting that the difficulties of SPH to follow the formation of KH instabilities depend not only on velocity noise, but also on the LMI (Agertz et al. 2007; Price 2008; Read et al. 2010; Valcke et al. 2010). This LMI occurs because, in the presence of a density step, the entropy conservation of SPH causes a pressure blip at the boundary. These pressure discontinuities in turn lead to the presence of shock waves, which then inhibit the growth of KH instabilities (Valcke et al. 2010).

Different approaches have been taken to eliminate or reduce the LMI: by introducing initial conditions with a smoothing of the density step (Valcke et al. 2010), and/or adding an AC term to give smooth entropies (Price 2008), or by reformulating the SPH density estimate (Ritchie & Thomas 2001).

Based on a suite of numerical tests, Valcke et al. ([2010]) argued that for low Mach numbers ($M \lesssim 0.2$) the growth of KH instabilities is still suppressed by the LMI. Although the magnitude of the shocks induced by LMI has been greatly reduced because of the initial density smoothing, Valcke et al. ([2010]) found that for low M the timescales τ_{KH} are much higher than those set by the numerical shocks.

It is not trivial to remove from the simulations these residual shocks. For instance, they can be eliminated by applying a relaxing scheme to the initial conditions, but the growing KH instabilities are then strongly suppressed by the induced particle disorder (Valcke et al. [2010]). A study on these effects is beyond the scope of this paper.

As a final point, it must be stressed that the results of the KH runs presented here have been obtained by using the AV scheme of Section [2.2] with settings AV_2. By replacing this scheme with the AV switch of Cullen & Dehnen ([2010]), we expect a significant reduction in the amount of AV present in the simulations (see the results of the previous and the next section). This, in turn, will result in a more inviscid behavior and a better capacity of the code to follow the development of the KH instabilities.

4.3. Subsonic Turbulence

Studies of driven isothermal subsonic turbulence (Bauer & Springel [2012]) have shown substantial differences in the properties of the velocity power spectra extracted from mesh-based simulations, when compared with those produced from the same test runs using the standard formulation of SPH.

Although the use in standard SPH of a time-dependent AV scheme alleviates the problem (Price [2012b]), the discrepancies are still present and their origin has been identified as being due to large errors in the SPH gradient estimates (Bauer & Springel [2012]). These errors in turn imply the presence of subsonic velocity noise, which is higher as lower Mach numbers are considered. As a result, SPH simulations exhibit spectra with a much smaller inertial range (i.e., Kolgomorov-like) than the ones measured using mesh codes.

A faithful numerical modeling of subsonic turbulence is particularly relevant in various astrophysical contexts (star formation, intracluster medium, intergalactic medium), and it is therefore important to investigate the capability of the IA scheme to properly simulate this test problem.

To this end we set an HCP lattice of N^3 particles with initially zero velocities inside a periodic box of sidelength $L = 1$ and density $\rho = 1$. The gas was isothermal with $\gamma = 1$ and $c_s = 1$. Turbulence in the gas was driven by adding to the momentum Equation ([3]) of the particles an external stochastic driving force a_{stir}. This was constructed in k-space according to a procedure already used by previous authors (Price & Federrath [2010]; Bauer & Springel [2012]; Price [2012b]; Hopkins [2013], [2015]; Zhu et al. [2015])

The power spectrum of $a(k)_{stir}$ varies as $P(k) \propto k^{-5/3}$ and the Fourier modes are non-zero in the range between $k_{min} = 2\pi/L$ and $k_{max} = 2k_{min}$. The phases of the stirring field are drawn from an Ornstein-Uhlenbeck (UO) process for which the random sequence at the step n is given by (Eswaran & Pope [1988]; Bartosch [2001])

$$x_{n+1} = fx_n + \sigma\sqrt{1 - f^2} z_n, \tag{44}$$

where $f = \exp(-dt/t_s)$ is a decaying factor, z_n is a Gaussian random variable with unit variance and σ is the variance of the

UO process. The constructed sequence then has $\langle x_n \rangle = 0$ and $\langle x_{n+1}x_n \rangle = \sigma^2 f$.

In order to obtain a pure solenoidal driving, we apply a Helmholtz decomposition in k space:

$$a_i(k, t) = b_i(k, t) - k_i(\boldsymbol{b} \cdot \boldsymbol{k})/k^2, \tag{45}$$

where the vector $\boldsymbol{b}(\boldsymbol{k})$ is a complex vector-valued stochastic process characterized at any given $\boldsymbol{k}$ by 6 UO random sequences ([44]) and $\boldsymbol{a}$ is the solenoidal stirring field ($\boldsymbol{a} \cdot \boldsymbol{k} = 0$).

The particle accelerations are calculated at each timestep by updating the stochastic field according to the described procedure, the summation in k space being performed by summing directly at the particle positions. For the driving parameters, we use the values of Bauer & Springel ([2012], Table 1). The power spectrum is normalized so that the rms Mach number $\mathcal{M}$ lies in the range of $\mathcal{M} \sim 0.25 - 0.3$ after the simulations have reached the steady-state regime ($t \gtrsim 5$).

We compared results extracted from subsonic simulations performed with the standard and IA implementations of SPH. We ran simulations with three different resolutions: $N^3 = 64^3$, 128^3, and $N = 256^3$. For a given resolution, we used in both of the schemes the same initial condition setup and stirring force field. In all of the simulations, we ran up to $t = 50$ and adopted the $M5$ kernel with $N_n = 50$ neighbors. We perform standard and IA runs by using the time-dependent AV scheme of Section [2.2] with settings AV_2. Additionally, we also run a set of IA simulations by using the AV method of Cullen & Dehnen ([2010]). In the following, we will refer to these IA runs with the term IA-CD, while we will use the term IA-AV when referring to the IA runs with AV settings AV_2.

As in other works (Bauer & Springel [2012]; Hopkins [2015]), we measure the spectral properties of the turbulent velocity field to assess the performances of the two codes. The velocity power spectrum is defined as

$$E(k) = 2\pi k^2 \mathcal{P}(k), \tag{46}$$

where $k \equiv |\boldsymbol{k}|$, and $\mathcal{P}(k)$ is the ensemble average velocity power spectrum. This is given by

$$\langle \tilde{\boldsymbol{u}}^\dagger(\boldsymbol{k}')\tilde{\boldsymbol{u}}(\boldsymbol{k}) \rangle = \delta_D(\boldsymbol{k}' - \boldsymbol{k})\mathcal{P}(k), \tag{47}$$

where $\tilde{\boldsymbol{u}}(\boldsymbol{k})$ is the Fourier transform of the velocity field $\boldsymbol{u}(\boldsymbol{x})$:

$$\tilde{\boldsymbol{u}}(\boldsymbol{k}) = \frac{1}{(2\pi)^3}\int \boldsymbol{u}(\boldsymbol{x})e^{-\imath 2\pi \boldsymbol{k}\cdot\boldsymbol{x}}d^3x. \tag{48}$$

In the case of incompressible turbulence, the energy spectrum follows the Kolgomorov scaling $E(k) \propto k^{-5/3}$. To measure the energy spectrum, we first set inside the simulation box a cube with $N_g = (2N)^3$ grid points. From the particle velocities $\boldsymbol{u}(\boldsymbol{x}_i)$, we then estimate the grid velocity field $\boldsymbol{u}(\boldsymbol{x}_g)$ at the grid points $\boldsymbol{x}_g$, using a triangular-shaped cloud function interpolation scheme.

We then compute the discrete Fourier transforms of $\boldsymbol{u}(\boldsymbol{x}_g)$ and the discrete power spectrum $\mathcal{P}^d(k) = \langle |\tilde{\boldsymbol{u}}^d(\boldsymbol{k})|^2 \rangle$ is evaluated by binning the quantity $|\tilde{\boldsymbol{u}}^d(\boldsymbol{k})|^2$ in spherical shells of radius k and averaging in the bins. The energy density of Equation ([46]) is then given, aside from a normalization factor, by $E(k) = 2\pi k^2 \mathcal{P}^d(k)$. Finally, for a given simulation, the spectrum $E(k)$ is estimated by doing a time-average between $t = 10$ and $t = 25$, with the spectrum being sampled each $\Delta t = 0.08$ time interval.

We show in Figure [9] the spectra $E(k)$ as measured from our simulations. The spectral behavior of the standard runs is in
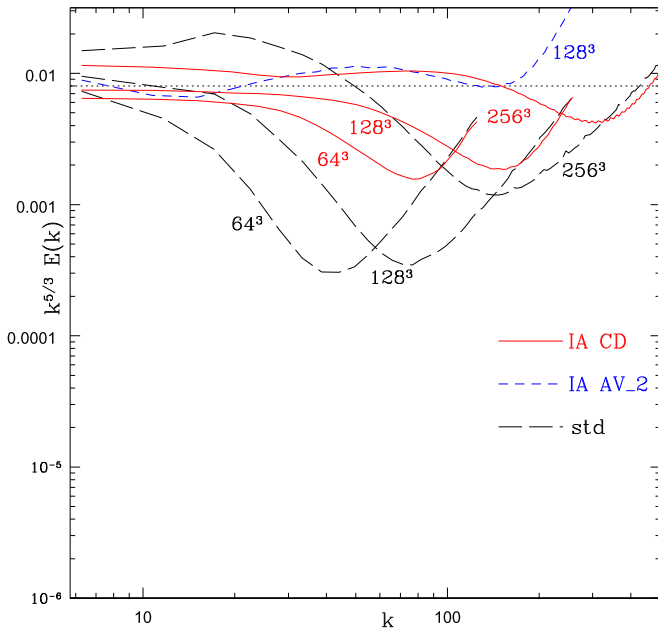
Figure 9. Time-averaged velocity power spectra of driven subsonic ($\mathcal{M} \sim 0.3$) isothermal turbulence. The spectra are compensated by $k^{5/3}$ so that the horizontal dotted line indicates the Kolgomorov scaling. We ran simulations using the same driving routine with $N^3 = 64^3$, 128^3 and $N = 256^3$. Dashed (black) lines are for the standard SPH runs, short-dash (blue) line is the $N^3 = 128^3$ IA run with AV settings AV_2 (Section 2.2), solid (red) lines are the IA runs performed using the the AV switch of Cullen & Dehnen (2010).

broad agreement with previous findings (Bauer & Springel 2012; Price 2012b; Hopkins 2013, 2015; Zhu et al. 2015). The spectra are characterized by a very narrow inertial range at low wavenumbers, with a significant decline at higher k. The spectra reach a minimum at a wavenumber k_{turn}, which increases as higher resolutions are considered, followed by a steep increase in the power at smaller scales $k \gtrsim k_{turn}$.

The precise value of $k_{turn} \sim 40$–200 depends on N, but it is still much smaller than the noise scale $\sim 2h_{max}$ set by the kernel. For incompressible turbulence, one can easily approximate h_{max} with the value of $\overline{h}$ given by the average density, thus obtaining $2\pi/2\overline{h} \sim \pi\zeta (N/L) (4\pi/3N_n)^{1/3} \sim 220 (N/64) \gg k_{turn}(N)$.

According to Price (2012b), the very limited capability of standard SPH to develop a Kolgomorov-like spectrum is due to the excess of numerical viscosity present in the scheme, which can be reduced by adopting a time-dependent AV switch.[3] In contrast, Bauer & Springel (2012, Figure 6) showed that the rise in power at small scales is mainly a result of the subsonic velocity noise due to kernel gradient errors present in standard SPH. For the same set of initial conditions and forcing sequence, their spectra extracted from runs performed using the moving-mesh code Arepo exhibit an inertial range, which extends over more than a decade in k. Similar results were later obtained by Hopkins (2015, their Figure 27), by using a completely different code (Gizmo) for the same test problem.

A similar behavior is found here for the spectra of the IA-CD runs depicted in Figure 9, which show a dramatic improvement over the corresponding standard SPH runs. The spectra now exhibit a much larger inertial range, which increases with resolution and for the $N = 256$ simulation it extends down

---

[3] We recall that with the term standard SPH, we refer here to the usual SPH scheme of Section 2.1, but incorporating the time-dependent AV switch described in Section 2.2.

to $k \sim 200$, close to the minimum scale $k_{max} \sim 2\pi N/5$ estimated by Hopkins (2015). The spectra are similar to the corresponding ones shown in Figure 27 of Hopkins (2015), but with fluctuations that stay within a factor of approximately two for $k \lesssim k_{max}$.

The velocity power spectra of the IA-AV runs exhibit significant differences with respect to those of the corresponding IA-CD simulations. For the sake of clarity, in Figure 9, we show only the spectrum of the $N = 128$ run. This spectrum is characterized by a significant amount of noise, with a departure from its parent IA-CD run, which already begins at scales above the Nyquist frequency.

This sensitivity of the IA spectra on the adopted AV scheme is at variance with what is seen in the SPH (TSPH and PSPH) runs of Hopkins (2015), in which the impact of AV on spectral behavior is not so significant. We interpret this strong dependence of velocity power spectra on the AV scheme as being due to the effectiveness of the IA method in removing gradient errors. This in turn implies that AV, which was previously subdominant (Bauer & Springel 2012), is now the main source of noise. The level of noise seen in the IA-AV spectra is then absent in the spectra of the IA-CD runs, because of the limited amount of AV that is generated by the employed AV switch.

Finally, in Figure 10, we show 2D maps of the density ρ, velocity $\boldsymbol{v}$, and $|\boldsymbol{\nabla} \times \boldsymbol{v}|^2$ extracted at $t = 50$ from simulations with a resolution of $N^3 = 128^3$ for both IA and standard SPH runs. A visual comparison between the maps of the two runs clearly indicates the presence in the IA simulation of well-resolved small-scale features, which are absent in the corresponding standard SPH map. These features of the IA maps appear qualitatively very similar to those obtained, in their tests on subsonic turbulence, by Bauer & Springel (2012, their Figure 4) and by Hopkins (2015, their Figure 26).

These findings confirm that, in SPH simulations, kernel gradient errors play a key role in the modeling of subsonic turbulence, and demonstrate how the IA scheme can be profitably used to overcome these difficulties, with results that compare well with those obtained with other numerical schemes recently proposed.

4.4. Keplerian Disk

The cold Keplerian disk problem has been investigated by many authors (Imaeda & Inutsuka 2002; Cartwright et al. 2009; Cullen & Dehnen 2010; Hu et al. 2014; Hopkins 2015; Schaal et al. 2015; Hosono et al. 2016; Pakmor et al. 2016). The test consists of a gaseous disk orbiting around a point-like mass. The disk has negligible pressure and its self-gravity is neglected; the disk is then in equilibrium with the centrifugal forces being balanced by the gravity of the central mass. Because of these conditions, the system is in a steady state and the initial disk configuration should remain stable as a function of time.

For SPH codes, this problem is very challenging, since even a small amount of AV causes a transport of angular momentum leading to particle disorder and disk break-up. The problem is particularly severe in the inner part of the disk, where the differential rotation causes strong shear flows.

In SPH, suppression of AV in the presence of shear flows is regulated by the Balsara switch (8). Because of this, higher order velocity gradient estimators must be adopted (Cullen & Dehnen 2010) in order to prevent or delay the disk instability
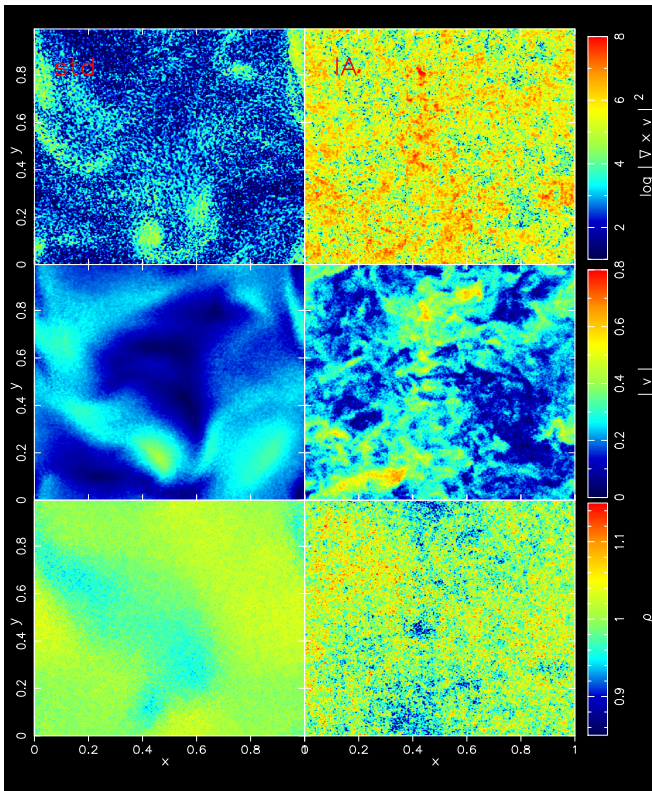
Figure 10. 2D maps of the density (bottom), velocity (middle), and enstrophy (top) fields extracted from simulations of driven subsonic turbulence with resolution $N^3 = 256^3$ and at the time $t = 25$. The left column is for standard SPH and the right column refers to the IA runs. The fields are evaluated on a grid of 512^2 points located at $z = L/2$; an SPH interpolation procedure is used to compute field values from particle quantities at grid points.

in SPH runs. Additionally, because pressure forces are very small, zeroth-order errors in hydrodynamic forces can also play a role in developing instabilities. It is therefore interesting to investigate the performance of the proposed IA scheme with the cold Keplerian disk problem.

We implement our initial conditions in a manner similar to that of previous authors (Hopkins 2015; Schaal et al. 2015). More specifically, we set up the disk in a three-dimensional periodic domain with boundaries defined by $\{-2.5, -2.5, 0\} \leqslant x, y, z < \{2.5, 2.5, 0.25\} \equiv \{L_x/2, L_y/2, L_z\}$. Within this domain, the disk density satisfies

$$\rho(r) = \begin{cases} 1 & 0.5 \leqslant r \leqslant 2 \\ 0 & 2 < r, \end{cases} \qquad (49)$$

where r is the cylindrical radius $r = \sqrt{x^2 + y^2}$.

Unlike in previous settings (Hopkins 2015; Schaal et al. 2015), here the disk edges are unsmoothed, moreover, we put in the x–y plane a small empty zone around the disk to avoid border effects so as to mimic vacuum boundary conditions. The gas initially has a very small constant pressure, $P = 10^{-6}$, and index $\gamma = 5/3$.

For the central point mass, we set $GM = 1$ and the gas is subject to a static gravitational acceleration $\boldsymbol{a} = -\boldsymbol{\nabla}\Phi$, where $\Phi = -(r^2 + \epsilon^2)^{-1/2}$ is the softened potential. We introduce a softening parameter, $\epsilon = 0.25$, to avoid diverging accelerations for those particles that during the simulations escape the initial disk configuration and approach the origin at $r = 0$. The initial particle rotational velocity is then $V_\phi = r(r^2 + \epsilon^2)^{-3/4}$ and for

the Keplerian orbital period $T = 2\pi r^{3/2}$, we choose as reference value that at $r = 1$. Hereafter, we express time in units of $T = 2\pi$.

We implement the initial condition setup according to the following procedure. We first construct a uniform glass-like distribution of $256^2 \times 16$ particles inside a parallelepiped of side lengths $4 \times 4 \times 0.25$. This is done by creating 16×16 replicas of a root unit cube of 16^3 glass-like particles along each x and y axis. and then rescaling the parallelepiped. Finally, we only keep those particles whose (x,y) coordinates satisfy the conditions given in Equation (49). The final number of particles used in the simulations is then $N = 16 \times 256^2 \pi/4 \sim 8.2 \times 10^5$. The velocities of the particles are initialized consistently with their position. In all of the SPH runs, we use the same initial conditions setup and the kernel ($W4$) with $N_n = 200$ neighbors. The simulations are evolved up to a maximum time of $t = 20$.

It must be stressed that the capability of the code to follow the disk orbits depends sensitively of how the initial particle configuration has been chosen in order to minimize the growth of numerical instabilities (Cartwright et al. 2009). In this aspect, after several tests, it has been found that the most stable disks are obtained when a glass-like particle distribution is used to realize the density setup (49).

For some of the simulations performed, we show in Figure 11 density maps of the simulated disks at various times. The maps are 2D slices calculated on an 800×800 grid located at $z = L_z/2$ in the simulation domain.

We do not show here results from disk simulations performed with the standard SPH implementation; these are in line with previous findings and the disk is found to be subject to disruption after a few orbits ($t \sim 2$–3). Introducing the IA scheme significantly improves the code capability for evolving the disk, which now can be followed up to $t \sim 15$ before it begins to degrade (Figure 11, left and middle panels).

This SPH simulation (IA-AV$_5$) was performed by setting $\{\alpha_{min}, \alpha_{max}, l_d\} = \{0.01, 1.5, 1.0\}$ for the AV parameters, this choice being indicated with the notation AV$_5$ in previous calibration tests (Valdarnini 2011). With respect to the set of AV parameters adopted in the other tests performed here (AV$_2$), the setting AV$_5$ is characterized by a very low floor value ($\alpha_{min} = 0.01$) and the shortest possible decay timescale ($l_d = 1.0$). This choice of AV parameters in SPH runs, improves the disk stability, though not in a significant way, with disk break-up occurring at $t \sim 12$ when the setting AV$_2$ is used.

Moreover, it must be stressed that in the IA runs the velocity divergence and vorticity are calculated from a velocity gradient matrix, in accordance with the adopted IA scheme. The results presented here are, however, still valid if a standard SPH estimator is used in the calculation of the velocity gradients, with disk stability being affected only marginally. This shows that errors in hydrodynamic forces are dominant in determining disk stability, with respect to low-order errors affecting the shear viscosity limiter (8).

A significant improvement in disk stability is obtained by replacing the time-dependent AV scheme of Section 2.2 with the improved method proposed by Cullen & Dehnen (2010), which is still based on the Morris & Monaghan (1997) scheme but has a better shock indicator and a more accurate AV limiter.

An IA-SPH simulation (IA-CD) performed by incorporating the new AV scheme shows that the small amount of AV, which still affected disk evolution in the IA-AV$_5$ run, is now removed
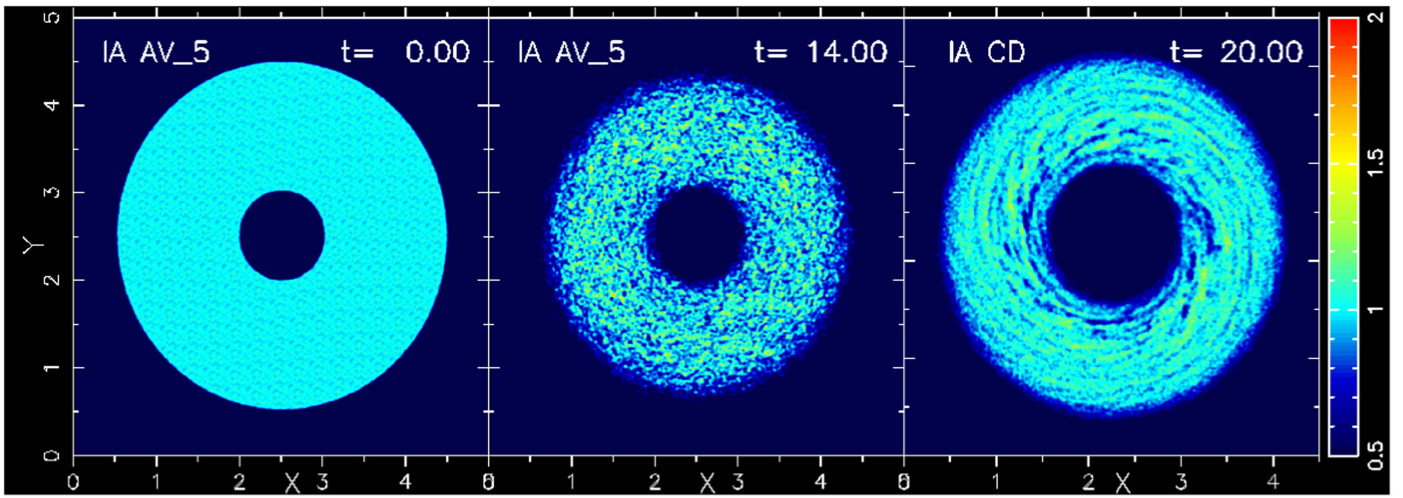
Figure 11. For some of the SPH runs, we here show at various times (in units of $T = 2\pi$), 2D density maps of the Keplerian disk. All of the SPH simulations incorporate the IA scheme, the code velocity divergence and vorticity being calculated in accordance with the scheme. Left: initial configuration for an SPH simulation that uses the AV setting $\{\alpha_{min}, \alpha_{max}, l_d\} = \{0.01, 1.5, 1.0\}$ (see Section 2.2). Middle: the same simulation but at $t = 14$. Right: here we show at $t = 20$ the disk density for an SPH run in which the AV scheme being used is that of Cullen & Dehnen (2010). To better discriminate disk structure in this run, the size of the computational domain has been reduced to $L_x = L_y = 4.5$.

and the disk structure is now stable up to 20 orbits. The disk density map of the IA-CD run is shown at $t = 20$ in the right panel of Figure 11, and can be compared with the corresponding density maps shown in Figure 6 of Hopkins (2015).

A comparison between the two suites of simulations is possible because we adopt here the same initial condition setup. In previous papers (Hu et al. 2014; Beck et al. 2016), the Gaussian ring version of the problem has been used to test new versions of SPH, but we expect our conclusions to remain unaffected by our choice of initial conditions.

To summarize, the results presented here for the Keplerian disk problem demonstrate that for an SPH code both errors in gradient accuracy and the level of AV contribute to disk stability, with the former having a much greater impact.

5. CONCLUSIONS

In this paper, we have investigated the performance of an improved version of the standard SPH formulation, in which an integral approach is used to strongly reduce zeroth-order errors in gradient estimates.

The IA method has been proposed and tested in a variety of hydrodynamical test problems (García-Senz et al. 2012; Rosswog 2015), but its most significant applications are in the simulation of subsonic flows. In the low Mach number regime, the difficulties of standard SPH have been found to be particularly severe (Bauer & Springel 2012; Dehnen & Aly 2012; García-Senz et al. 2012; McNally et al. 2012; Valdarnini 2012; Hopkins 2015) and gradient accuracy is a key prerequisite for accurately modeling the fluid dynamics.

Given the advantages of a numerical hydrodynamical scheme based on a Lagrangian formulation (for instance its natural resolution adaptativity) it is therefore crucial to assess the capability of the proposed IA-SPH scheme to handle subsonic flows. Moreover, the IA method retains the fully conservative nature of the Lagrangian SPH scheme, unlike previous attempts aimed at removing zeroth-order gradient errors present in SPH.

To evaluate code performance, we have analyzed results from a suite of simulations of hydrodynamical test problems, performed using both the IA and standard SPH formulations. We also contrast the accuracy of the results with that produced by new numerical schemes (Springel 2010; Bauer & Springel 2012; Hopkins 2015), against which standard SPH has been found clearly inadequate. Our main conclusions are as follows.

For the Gresho–Chan vortex problem, it is well known (Dehnen & Aly 2012; Read & Hayfield 2012; Hu et al. 2014; Hopkins 2015) that standard SPH is heavily affected by the E_0 error and the code performances are very poor. On the contrary, the IA formulation leads to much better behavior, with the results of Section 4.1 being in line with those obtained by other numerical schemes (Springel 2010; Hopkins 2015).

The resolution study displayed in Figure 3 shows for the $L1$ velocity error a gain in accuracy by a factor ~ 10 over standard SPH. Moreover, the validity of the approach is confirmed even in the regime of very cold flows. This is demonstrated by the velocity profiles of Figure 4, in which the code is shown to be able to reproduce the analytic solution for the azimuthal velocity down to $M = 0.02$.

The results of Section 4.2 on KH tests also indicate how zeroth-order errors present in SPH affect the growth of KH instabilities and the effectiveness of the IA scheme in reducing these errors. Nonetheless, in the very low subsonic regimes, the IA method shows, at a fixed resolution, a progressively reduced capability to follow the development of the instability. This is not surprising since, for the chosen settings, by reducing the Mach number the perturbation amplitude is also reduced and it becomes progressively more challenging, keeping the resolution fixed, to simulate the KH instability when $M \lesssim 0.1$.

In this respect, the heuristic arguments used in Section 4.2 to derive the necessary resolution give a lower limit for N, which, in any case, should be taken with caution, with the required value probable being much higher. In fact, to the author's knowledge, KH simulations with very low Mach numbers ($M \lesssim 0.1$) have not previously been undertaken in the literature and it would be interesting to compare the findings of Section 4.2 with the behavior of a mesh-based code in these regimes.

The good performances of the IA formulation are confirmed by the results of Section 4.3 on simulations of driven subsonic turbulence, for which the failure of standard SPH to properly model this problem has been debated by various authors (Bauer & Springel 2012; Price 2012b; Hopkins 2013, 2015; Zhu et al. 2015). Simulations performed employing the new scheme produce velocity spectra in better agreement with the Kolgomorov law and exhibit an inertial range that now covers nearly a decade (Figure 9). Here again we see how the results, for the same initial setting and resolution, do not differ significantly from those produced by other codes (Bauer & Springel 2012; Hopkins 2015).

In the Keplerian disk problem, suppression of numerical viscosity is a critical factor for achieving stable evolution. However, the results of Section 4.4 also show errors in hydrodynamical forces having a significant impact on disk stability. This suggests that the instabilities leading to disk disruption are sourced by a combination of these two factors. To successfully simulate this test problem, an SPH code must then be necessarily based on both the IA scheme and the improved AV switch of Cullen & Dehnen (2010).

The use of an IA scheme within an SPH framework also raises the issue of revisiting the choice of the kernel in SPH simulations. As discussed in Section 3, the introduction of Wendland kernels stems from the necessity of avoiding pairing instability. However, this problem arose from the need to reduce zeroth-order errors present in standard SPH, which are absent or very small in the IA scheme. Therefore, if one adopts the IA-SPH framework, one can resort to the use of the M_5 or M_6 splines in place of the Wendland kernels. This choice is motivated, for the same number of neighbors, by the better accuracy of the B-splines in estimating densities, when contrasted against the Wendland kernels (see Section 3).

To summarize, the results of our tests demonstrate that by incorporating the IA method in standard SPH, the zeroth-order errors in the momentum equations are drastically reduced, with significant improvements in the performance of the new code.

These results are particularly significative given the importance of subsonic flows in many astrophysical problems. For example, in galaxy clusters subsonic turbulence adds a contribution to the intracluster medium pressure, thus biasing cluster mass estimates and in turn affecting the use of clusters as cosmological probes (Brüggen & Vazza 2015, and references cited therein).

We thus conclude that the new IA-SPH scheme, being based on a Lagrangian formulation, can be profitably used in those simulations of subsonic astrophysical flows in which the shortcomings of standard SPH prevented the full exploitation of its resolution adaptativity and conservation properties.

REFERENCES

Abel, T. 2011, MNRAS, 413, 271
Agertz, O., Moore, B., Stadel, J., et al. 2007, MNRAS, 380, 963
Aguilar, J. C., Berriel-Valdos, L. R., & Aguilar, J. F. 2011, Proc. SPIE, 8011, 801186
Balsara, D. 1995, JCoPh, 121, 357
Bartosch, L. 2001, IJMPC, 12, 851
Bauer, A., & Springel, V. 2012, MNRAS, 423, 2558
Beck, A. M., Murante, G., Arth, A., et al. 2016, MNRAS, 455, 2110
Biffi, V., & Valdarnini, R. 2015, MNRAS, 446, 2802
Børve, S., Omang, M., & Trulsen, J. 2004, ApJS, 153, 447
Brookshaw, L. 1985, PASAu, 6, 207
Brüggen, M., & Vazza, F. 2015, in Astrophysics and Space Science Library, Vol. 407 ed. A. Lazarian et al. (Berlin: Springer), 599
Bryan, G. L., Norman, M. L., O'Shea, B. W., et al. 2014, ApJS, 211, 19
Cartwright, A., Stamatellos, D., & Whitworth, A. P. 2009, MNRAS, 395, 2373
Cha, S.-H., Inutsuka, S.-I., & Nayakshin, S. 2010, MNRAS, 403, 1165
Cullen, L., & Dehnen, W. 2010, MNRAS, 408, 669
Dehnen, W., & Aly, H. 2012, MNRAS, 425, 1068
Dilts, G. 1999, IJNME, 44, 1115
Duffell, P. C., & MacFadyen, A. I. 2011, ApJS, 197, 15
Eswaran, V., & Pope, S. B. 1988, CF, 16, 257
Fryxell, B., Olson, K., Ricker, P., et al. 2000, ApJS, 131, 273
García-Senz, D., Cabezón, R. M., & Escartín, J. A. 2012, A&A, 538, A9
García-Senz, D., Cabezón, R. M., Escartín, J. A., & Ebinger, K. 2014, A&A, 570, A14
Gingold, R. A., & Monaghan, J. J. 1977, MNRAS, 181, 375
Gresho, P. M., & Chan, S. T. 1990, IJNMF, 11, 621
Heß, S., & Springel, V. 2010, MNRAS, 406, 2289
Hernquist, L., & Katz, N. 1989, ApJS, 70, 419
Hopkins, P. F. 2013, MNRAS, 428, 2840
Hopkins, P. F. 2015, MNRAS, 450, 53
Hosono, N., Saitoh, T. R., & Makino, J. 2016, ApJS, 224, 32
Hu, C.-Y., Naab, T., Walch, S., Moster, B. P., & Oser, L. 2014, MNRAS, 443, 1173
Imaeda, Y., & Inutsuka, S.-i. 2002, ApJ, 569, 501
Inutsuka, S.-I. 2002, JCoPh, 179, 238
Junk, V., Walch, S., Heitsch, F., et al. 2010, MNRAS, 407, 1933
Kawata, D., Okamoto, T., Gibson, B. K., Barnes, D. J., & Cen, R. 2013, MNRAS, 428, 1968
Kravtsov, A. V., Klypin, A. A., & Khokhlov, A. M. 1997, ApJS, 111, 73
Liu, M. B., Liu, G. R., & Lam, K. Y. 2003, JCoAM, 155, 263
Lucy, L. B. 1977, AJ, 82, 1013
McNally, C. P., Lyra, W., & Passy, J.-C. 2012, ApJS, 201, 18
Miczek, F., Röpke, F. K., & Edelmann, P. V. F. 2015, A&A, 576, A50
Mitchell, N. L., McCarthy, I. G., Bower, R. G., Theuns, T., & Crain, R. A. 2009, MNRAS, 395, 180
Monaghan, J. J. 1997, JCoPh, 136, 298
Monaghan, J. J. 2005, RPPh, 68, 1703
Morris, J. P. 1996, PASA, 13, 97
Morris, J. P., & Monaghan, J. J. 1997, JCoPh, 136, 41
Murante, G., Borgani, S., Brunino, R., & Cha, S.-H. 2011, MNRAS, 417, 136
Norman, M. L. 2005, in Adaptive Mesh Refinement—Theory and Applications, vol. 41 ed. T. Plewa, T. Linde, & V. G. Weirs (Berlin, New York: Springer), 413
Norman, M. L., & Bryan, G. L. 1999, in Numerical Astrophysics, Vol. 240 ed. S. M. Miyama, K. Tomisaka, & T. Hanawa (Boston: Kluwer), 19
O'Shea, B. W., Bryan, G., Bordner, J., et al. 2005, in Adaptive Mesh Refinement—Theory and Applications, Vol. 41 ed. T. Plewa, T. Linde, & V. G. Weirs (Berlin; New York: Springer), 341
Pakmor, R., Springel, V., Bauer, A., et al. 2016, MNRAS, 455, 1134
Price, D. J. 2008, JCoPh, 227, 10040
Price, D. J. 2012a, JCoPh, 231, 759
Price, D. J. 2012b, MNRAS, 402, L33
Price, D. J., & Federrath, C. 2010, MNRAS, 406, 1659
Read, J. I., & Hayfield, T. 2012, MNRAS, 422, 3037
Read, J. I., Hayfield, T., & Agertz, O. 2010, MNRAS, 405, 1513
Ritchie, B. W., & Thomas, P. A. 2001, MNRAS, 323, 743
Robertson, B. E., Kravtsov, A. V., Gnedin, N. Y., Abel, T., & Rudd, D. H. 2010, MNRAS, 401, 2463
Rosswog, S. 2009, NewAR, 53, 78
Rosswog, S. 2015, MNRAS, 448, 3628
Saitoh, T. R., & Makino, J. 2013, ApJ, 768, 44
Schaal, K., Bauer, A., Chandrashekar, P., et al. 2015, MNRAS, 453, 4278

Springel, V. 2005, MNRAS, 364, 1105
Springel, V. 2010, MNRAS, 401, 791
Springel, V., & Hernquist, L. 2002, MNRAS, 333, 649
Stone, J. M., Gardiner, T. A., Teuben, P., Hawley, J. F., & Simon, J. B. 2008, ApJS, 178, 137
Stone, J. M., & Norman, M. L. 1992, ApJS, 80, 753
Tasker, E. J., Brunino, R., Mitchell, N. L., et al. 2008, MNRAS, 390, 1267
Teyssier, R. 2002, A&A, 385, 337

Valcke, S., de Rijcke, S., Rödiger, E., & Dejonghe, H. 2010, MNRAS, 408, 71
Valdarnini, R. 2011, A&A, 526, A158
Valdarnini, R. 2012, A&A, 546, A45
Wadsley, J. W., Stadel, J., & Quinn, T. 2004, NewA, 9, 137
Wadsley, J. W., Veeravalli, G., & Couchman, H. M. P. 2008, MNRAS, 387, 427
Wendland, H. 1995, Adv. Comp. Math., 4, 389
Zhu, Q., Hernquist, L., & Li, Y. 2015, ApJ, 800, 6